River Water Surface Velocity Measurement Using Large-Scale Particle Image Velocimetry

By

Erwin Sy

A Thesis Submitted to the Faculty of Graduate Studies of

The University of Manitoba

In Partial Fulfillment of the Requirements of the Degree of

MASTER OF SCIENCE

Department of Mechanical Engineering

The University of Manitoba

Winnipeg

Abstract

It is proposed to use advancements in Large Scale Particle Image Velocimetry (LSPIV), such as improved charge-coupled device in cameras, unmanned aerial vehicles, and faster algorithms, for a non-invasive river water surface velocity measurement to assess potential hydrokinetic turbine sites. The approach will compare results to an Acoustic Doppler Velocimeter (ADV). Being able to measure the water surface velocity using the proposed method allows the use of a low-cost and simple approach to determine hydrokinetic sites suitable for turbine deployment for electrification of remote communities. The research tests were conducted in a water tunnel and at the Canadian Hydrokinetic Turbine Testing Center located in Winnipeg River using cameras and a drone with results compared to an ADV. Two LSPIV simulation software's PIVlab and OpenPIV were used to analyze the water surface velocity captured in a water tunnel and at the Canadian Hydrokinetic Turbine Testing Center. The results of the LSPIV software analysis with optimized average velocity data results from PIVlab are within ±0.1 m/s from the average ADV velocity results. In addition, optimized velocity data from PIVlab show vector results moved closer to the ADV measured water surface velocity and resulted with fewer fluctuations after the erroneous data was removed. Thus, a non-invasive way of analyzing water surface velocity by flying a drone overhead capturing the water surface and using LSPIV software such as PIVlab and OpenPIV to extract data from the captured images could replace conventional invasive methods of water surface velocity measurements for site assessments so long as these are done in good weather, minimal wind and water surface ripples are clear, detailed and defined.

Acknowledgements

I would like to start by thanking my adviser Dr. Eric Bibeau for giving me an opportunity to work with him. His mentorship and patience with me throughout the research process until my thesis completion have been invaluable. I would also like to thank Zeev Kapitanker and Kirk Dyson for giving advice and helping with the deployment of our equipment at the CHTTC center. Finally, on a personal level, I would like to thank my parents Tan Bee Ling and Juanito Sy, my brother James Sy, and my kids Brianne and Hanz Sy for their support. I would not have been able to complete the project without them giving me consistent comfort throughout the process.

Table of Contents

List of Figures

List of Tables

Abbreviations

ADV	Acoustic Doppler Velocimetry
AOI	Area of Interest
CC	Cross-Correlation
CHTTC	Canadian Hydrokinetic Turbine Testing Center
CLAHE	Contrast Limited Adaptive Histogram Equalization
CPU	Central Processing Unit
DPIV	Digital Particle Image Velocimetry
fps	frames per second
GCP	Ground Control Point
GHG	Greenhouse Gas
GSD	Ground Sampling Distance
GUI	Graphical User Interface
IA	Interrogation Area
KE	Kinetic Energy
LSPIV	Large Scale Particle Image Velocimetry
m/s	meter per second
ms	millisecond
PIV	Particle Image Velocimetry
ROI	Region of Interest
STIV	Space Time Image Velocimetry
UAV	Unmanned Aerial Vehicle

Chapter 1: Introduction

1.1 Energy usage

Greenhouse Gas (GHG) emitted by human activity is increasing mainly due to fossil fuel consumption, presently reaching 420 ppm [1]. As GHG increases in the Earth's atmosphere, it traps more heat; this in turn warms the earth [2]. There is ample evidence that this translates, for example, to more floods due to climate changes resulting from global warming [3]. Climate change is one of the most significant predicament that humanity must address and scientists conclude that this mainly from fossil fuel combustion and agriculture [4].

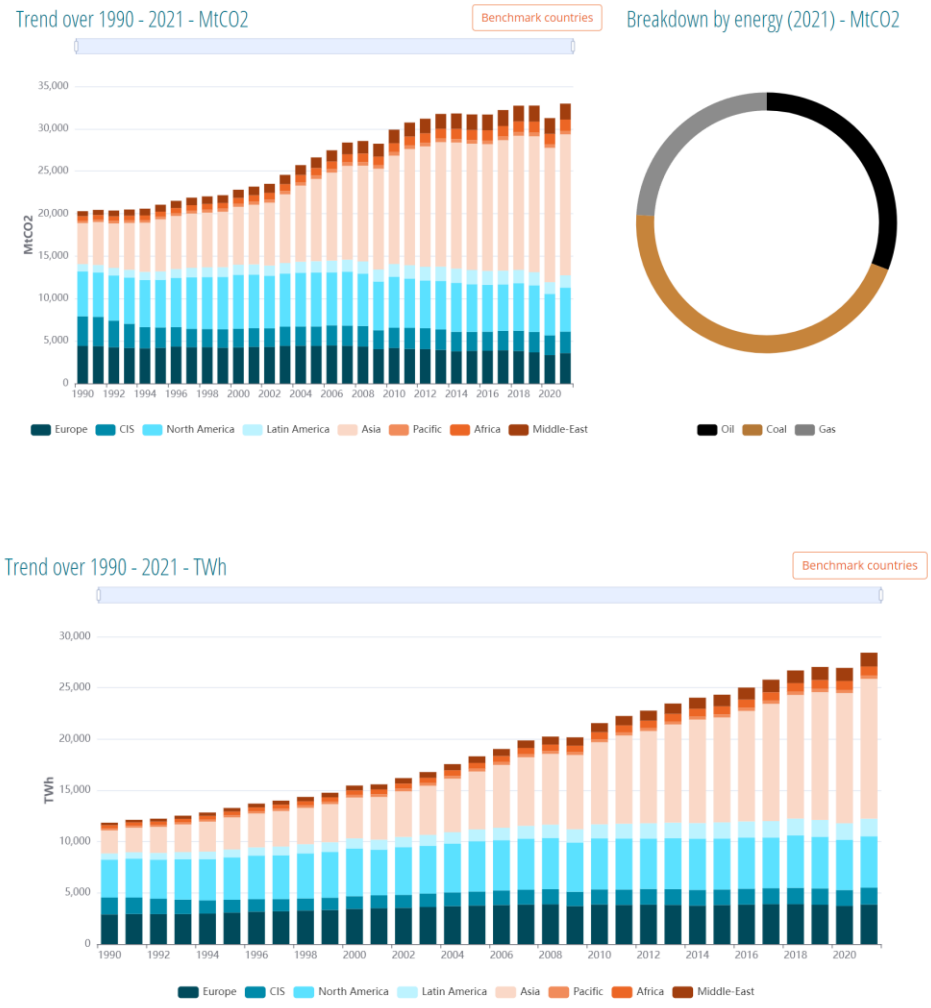

Figure 1: (a) CO_2 emissions, and (b) power generation from 1990 to 2021 [5]

Figure 1 shows electrical energy consumption increases with fossil fuel use, which in turn increases GHG. Moreover, fossil fuels are limited [6]: current proven fossil fuel reserves for oil are 50 years, coal 140 years, and natural gas 50 years, as summarized in Table 1.

Table 1: Proven fossil fuel reserves, rates of consumption, and lifetimes [7]

Fuel	Reserves (Q)	1995 Consumption (Q/Y)	Rate of Growth (%/y) 1987-1997	Lifetime (y) No Growth	Lifetime (y) with Growth
Coal	24,000	93	0.8	258	140
Oil	9,280	141	1.1	66	50
Gas	6,966	78	2.5	90	50

1.2 Renewable energy

Fossil fuel consumption is the leading cause for GHG increase [7]. Thus, limiting the use of fossil fuels and increasing the use of renewable energy in electricity production is critical to reducing GHG emissions [8]. There are many types of renewable energy sources: hydro, solar, wind, biomass, and geothermal. With Canada having an abundance of water resources, hydro is the natural choice for clean power generation. Currently, hydro provides more than 60% of Canada's electricity with an installed capacity exceeding 85 GW at present and 100 GW projected by 2035 [9].

The technology for extracting electric power from the kinetic energy of rivers is called River Hydrokinetic Turbines (RHT). Using RHT has some advantages over other renewable energy. For example, RHT energy provides a continuous supply of energy, could be an economical source of renewable energy [10], and is not affected by intermittency that affects solar and wind [11].

Kinetic energy is a property of river and wind currents [10]. The extraction of energy from both is similar with the main difference being in the density of the water being 800 times the density of air [8] [10] [12], the area of wind turbine is much larger, and the velocity of water being typically much less than air. The principle of HKT is converting the kinetic energy of water

flow to mechanical power by rotating the turbine generator to produce electricity, as shown in Figure 2.

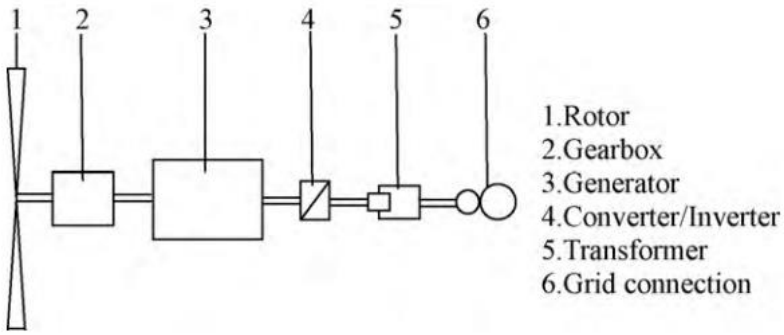

Figure 2: Principle of water turbine systems [10]

From physics, we know that the kinetic energy, KE, can be determined by

$$KE = \frac{1}{2}mv^2 \tag{1}$$

where m is the mass of the object and v is the velocity of the object. In fluid dynamics, the mass flow rate, ṁ, the density, ρ, and surface area, A, provides the available fluid power as [8]

$$P_{avail} = \frac{1}{2}\dot{m}v^2 \tag{2}$$

or

$$P_{avail} = \frac{1}{2}\rho A v^3 \tag{3}$$

To determine the power captured by the turbine, we need the upstream (V_i) and downstream (V_o) water velocities. This is given by:

$$P_o = \frac{1}{2}\,\dot{m}\,(V_i^2 - v_o^2) \tag{4}$$

If we assume that the fluid velocity is discontinuous at the turbine's vertical plane, the mass flow rate of the turbine can be approximated as

$$\dot{m} = \rho \cdot A_r \cdot \left(\frac{V_i + V_o}{2}\right) \tag{5}$$

and substituting gives the equation for maximum power for upstream fluid velocity [8]

$$P_{max} = \frac{1}{2} C_p \cdot \rho \cdot A_r \cdot V_i^3 \tag{6}$$

where C_p is the power coefficient constant and depends on the ratio of downstream to upstream fluid velocities (V_o/V_i). The C_p has a theoretical maximum value of 16/27 or 0.59 based on Betz law [13]. The Betz law stipulates the maximum achievable power that can be extracted from the kinetic flow to work or electrical energy [14]. Substituting the maximum C_p value to equation 6 gives us:

$$P_{max} = \frac{16}{27} \cdot \frac{1}{2} \cdot \rho \cdot A_r \cdot V_i^3 \tag{7}$$

Figure 3 shows the maximum theoretical limit of 59.3% for a single actuator disk [8], or the energy extracted from a surface which fluid flow.

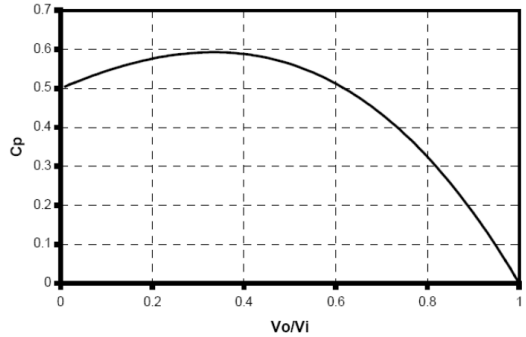

Figure 3: Power coefficient (C_p) versus upstream and downstream velocity ratios [8]

1.3 Large scale particle image velocimetry and HKT

Flow information and measurement in river basins is necessary in diverse applications that includes irrigation, flood control, power generation for placement of river hydrokinetic turbines, and water supply management [15] [16]. However, conventional velocity measurements methods can be difficult to carry out especially in more dangerous conditions such as floods [17].

Thus, imaging techniques such as Particle Image Velocimetry (PIV) has gained attention in the past decade [17] allowing measurements of surface velocity distributions accurately [18], safely and conveniently [19]. Eventually, PIV has been updated to measure the free surface of large bodies of water [20]. This is now called Large Scale Image Velocimetry (LSPIV). The foundation of the LSPIV technique is the use of the visible water surface texture as a passive tracer relative to the surface flow [16]. Thus, LSPIV can be used without adding tracers to water surface analysis [21].

Currently, Acoustic Doppler Velocimetry (ADV) is one of the most common and preferred acoustic instruments for water surface velocity measurements [22]. However, LSPIV is also a proven technique for measuring water surface velocities in rivers [23] and has advantages over acoustic instruments such as its near-instantaneous data collection [23], and its ability to create spatial resolutions that are similar to numerical models that will be difficult to achieve with acoustic instruments [22].

Recently, NRCan and the CHTTC have developed a radar satellite or synthetic aperture radar (SAR) method to find potential energetic river sites to locate HKT. This method has also been used to estimate the steams of the Han River basin in Korea using the European Space Agency Sentinel-1 satellite with great success [24]. The approach uses the fact that at velocities higher than approximately 1 m/s, energetic river sites do not freeze and have open water [25]. The radar satellite constellation settings are optimized to differentiate between ice and open water. After finding potential sites using satellites, a low-cost approach, like the LSPIV method, is then required to assess if the velocity at these sites is above 1.5 to 2 m/s which would then makes the site attractive to install HKT anywhere. This approach can be extended to track high

turbulence sections of rivers during monsoon season in warmer climates, making finding a low-cost method like LSPIV a critical path to find sites to install HKT worldwide as part of resource assessment.

Therefore, if satellites could identify sites above 1 m/s at low cost, we could then develop a low-cost approach to further investigate these sites (two-step approach).

1.4 Research goals / objectives

The objectives of this research are:

- Determine if a drone can be used to measure surface velocities at potential energetic river sites by processing recorded videos using open source LSPIV software.
- Determine the accuracy of using LSPIV to assess potential hydrokinetic sites to install HKT by comparing LSPIV to ADV.

1.5 Methodology

The proposed methodology in this research is to use laboratory and field experiments to find if LSPIV analysis would yield similar results to ADV measurements. Field experiments were first conducted at the Canadian Hydrokinetic Turbine Test Center (CHTTC) located on the Winnipeg River. The CHTTC site provided natural constant water flow, and amenities such as anchored buoys, boats, ADV's etc. essential for such experiment. The laboratory water tunnel allowed for a more controlled environment where no wind or other natural phenomena could affect the water flow. Water flow for the CHTTC and laboratory was filmed, and the video file was analyzed by an LSPIV simulation software. The process required filming at an angle called "nadir" thereby omitting orthorectification and enhancing water surface texture to improve surface ripple texture and visibility. To further improve data accuracy, inaccurate data such as those considered to be "too far" from the normal data results will be removed and replaced with interpolated data. Finally, resulting data from LSPIV and ADV are compared and analyzed. The flow methodology for the LSPIV analysis is shown in Figure 4.

1.6 Contribution and relevance of this research

Historically, the gold standard in river surface velocity measurement is to use invasive methods such as water buoys and current meters. Since then, new methods have been developed to measure river surface velocity. These methods use non-invasive new technologies such as LSPIV. However, most current research in this area requires seeding river systems, and orthorectification of images or captured video files. This study will strengthen the premise that the current advancements in civilian grade unmanned aerial vehicles coupled with built-in camera systems flown over open channel systems such as rivers can yield data that is comparable to current meters. This simplicity will allow faster river surface velocity measurement, while preventing the hazards that come with it. This contribution will open a new era of finding and measuring river surface velocities capable of driving HKT with its near instantaneous ability to deliver river surface velocity measurements, lowering the costs to survey, and making it safer for both researchers and personnel alike.

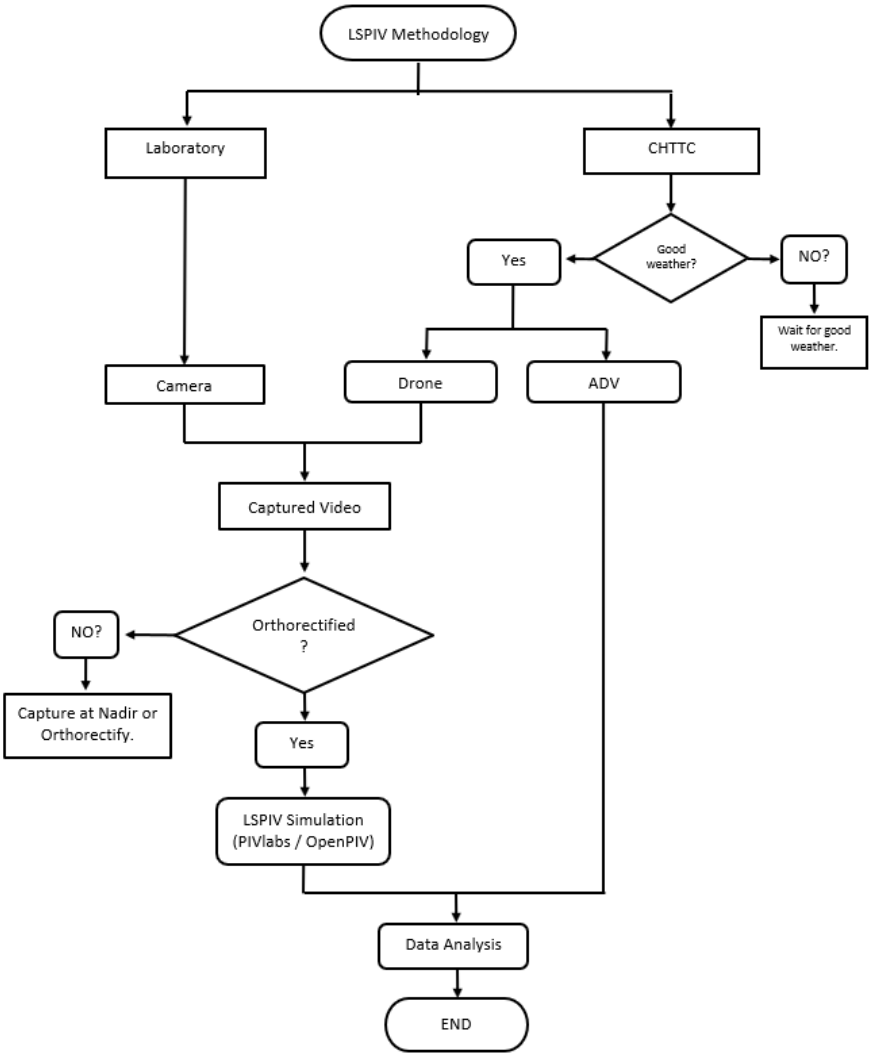

Figure 4: Methodology to achieve research objectives

Chapter 2: Literature review

This chapter will discuss the history of how LSPIV was conceptualized, how LSPIV is gaining traction as a dependable river surface velocity measurement tool, and how new technologies in imaging hardware and software have allowed LSPIV to produce reliable data. In addition, this section will go through the flow processing of LSPIV, discuss how site elements affect LSPIV analysis, and how new image enhancing algorithms are calculated with reduced errors yet requiring substantially less computational power.

2.1 Background

In 1977 Meynart used images to estimate water velocity and named his research Laser Speckle Velocimetry (LSV) [28]. In 1984, researchers Pickering, Halliwell and Adrian recognized the importance of particle images and created PIV to differentiate from LSV. Here, PIV will contain images of individual particles instead of a speckle pattern [18].

The rapid technological advancements in digital camera hardware and software [29], and better computer and digital technologies have removed problems associated with long processing and digitizing times for images [30]. Hence, the advancement and development of PIV has been accelerated with the advances in optical or imaging techniques [31].

Currently, there are five dominant ways to measure water surface velocity. They are floats, ADV, Acoustic Doppler Current Profiler (ADCP), radar, and image like LSPIV. Out the these, LSPIV is a good choice for open channel measurements for its instantaneous estimation of standard video equipment if there is sufficient illumination. Researchers have concluded that if the human eye can see the movement of the water surface, LSPIV can capture and quantify it [32]. Table 2 summarizes the methods.

Table 2: Comparison of selected characteristics of floats, acoustic, radar, and image-based velocimetry

	Floats	Acoustic (ADV, ADCP)	Radar	Image (LSPIV)
Technique	Intrusive	Intrusive	Non-intrusive	Non-intrusive
Measurement type	Buoys, floats.	Profile: along the acoustic beam path (verticals); three-component velocity [20].	Point: at the intersection of the beam with the free surface; one-component velocity [20].	Surface: instantaneous vector field at the free surface; two-component velocity [20].
Tracking method	Timer, tape measure	Small particles that are naturally suspended in the water column [20].	Small ripples generated by wind, or flow surplace on the water surface [20].	Foams, particles, debris, ice floes, and specular reflections on the free surface deformations (waves, boils, kolks). Added seeding. [20]
Limiting factor	Hard to put floats [16][19].	Instrument probe in contact with the flow. The flow assumed horizontally homogeneous [20].	The ratio between the Incident electromagnetic and water wave wavelengths within specified range. Instrument aligned with the dominant velocity [20].	Survey of minimum six points within the imaged area. Occasionally, additional seeding and illumination [20].
Output quality	Questionable when floats are trapped in Vortices [19].	Good spatial and temporal resolution. Inaccurate for very slow flows [20].	Limited spatial and temporal resolution. No reverse flows. Inaccurate for very slow flows [20].	Good spatial and temporal resolution [20].
Difficulty	Very difficult [19]	Difficult	Easy	Easy
Cost	Cheap	Expensive	Normal	Normal to cheap

2.2 Imaging techniques

The purpose of using video images in analyzing surface flow velocity is to allow surface velocity measurement safely and conveniently. Since surface video images contain visible flow textures such as surface ripples and floating objects that are advected with surface velocity, its velocity can then be measured if the wind effects are negligible [19].

Currently, there are two imaging techniques that are being applied to calculate surface velocities: These are: PIV, and the Space Time Image Velocimetry (STIV) [19] [33]. LSPIV is an updated PIV method that was developed to measure large surface flow fields such as rivers using particle tracking procedures [34]. STIV is a newer imaging technique that can also measure surface velocities on large surfaces but uses the direction of search lines extracted from the variation of brightness or the color on the water surface [35] from hundreds of images extracted from videos [36].

2.2.1 Comparison between LSPIV and STIV

As of current, LSPIV and STIV are the dominant imaging techniques used to extract surface velocities. However, both methods work on different principles. First, LSPIV's main principle for river surface velocity measurement is the use of patters that form on water surfaces as natural flow tracers with natural light as its main light source [19]. STIV, on the other hand, uses the gradients of gray level intensity [35] or the variation of brightness along the velocity measuring line in successive multiple images [19]. Second, LSPIV is a two-dimensional measurement whereas STIV is a one-dimensional measurement in the streamwise direction [19]. For example, LSPIV shows two-dimensional flow patterns within different hydrodynamic zones at each river confluence as well as the hydrodynamic conditions between the confluences [37]. Thus, LSPIV provides unprecedented spatial detail of two-dimensional pattern at confluences [37] whereas STIV will not be appropriate in this application since it is one-dimensional in the streamwise direction.

The final distinction is the speed of how data is processed. Fujita et al. performed sample calculations and the STIV method was almost ten times faster than LSPIV [35] in providing the same amount of information. The reason for this discrepancy is: First, LSPIV requires a large amount of information or recording space to store large-sized images, while STIV records only the Space Time Image (STI) for the search lines which requires little storage data [17]. Since LSPIV requires large amounts of information, a large storage memory and a powerful central processing unit are needed to calculate coefficients for pattern matching. This increases the cost of measurement and measurement time [38]. However, current LSPIV algorithms incorporate a discreet-Fourier transform that allows it to use significantly fewer resources and perform vector analysis faster [39]). Table 3 summarizes the general features of LSPIV and STIV.

Table 3: General feature of LSPIV and STIV [35]

	STIV	**LSPIV**
Concept	Gradient Measurement	Pattern Matching
Image Plane	2-D (in X-T plane)	2-D (in X-Y Plane)
Velocity Analysis	1-D (In-flow direction)	2-D (Free-Surface)
Spatial Resolution	High in Traverse	Less then STIV
Camera Setting	Random	Random
Image Noise	Robust	Less then STIV
Viewing Angle	Allow small angle	Require larger angle
CPU Usage	light	Intensive
System Construction	Easily Automated	Can be automated
Low Flow Measurement	feasible (use tracer)	feasible (use tracer)

2.3 LSPIV processing flow

LSPIV requires several procedures to process the captured video files into images that can be used to calculate the surface velocity. Figure 4 outlines these steps. First, a site is selected, and a date is determined when favorable weather conditions are expected. Then an Unmanned Aerial Vehicle (UAV) is flown and begins to film the area of interest (AOI). After the UAV finishes filming, the video file is imported to a Personal Computer (PC) for pre-processing. Pre-processing the video file by selecting a region of interest within the image file, removing unwanted areas in the image (also called masking), and altering the image file to enhance the picture. Finally, post-processing is done by calibrating the image, then optimizing data results by removing data that is inaccurate. Figure 5 summarizes the LSPIV flow process.

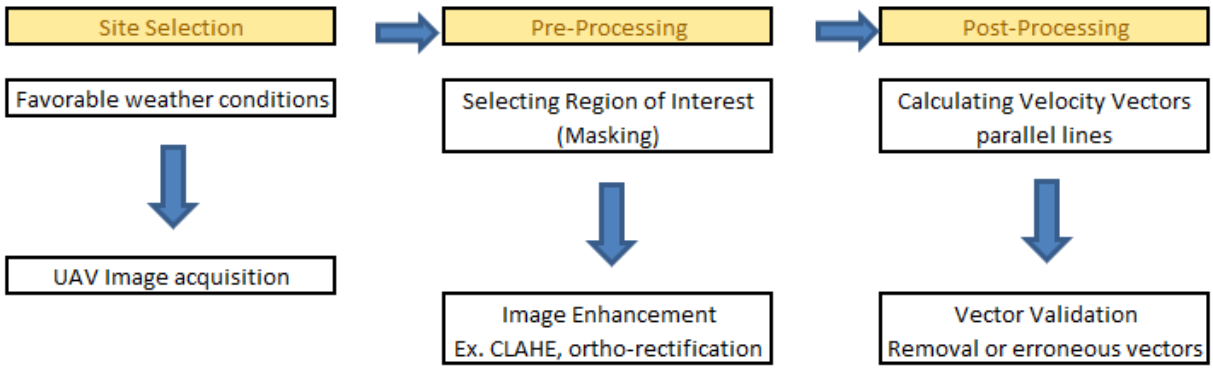

Figure 5: LSPIV process flow

2.3.1 Site selection

The site location conditions where video filming is done for LSPIV analysis is important inorder to yield accurate velocity data. First, conditions such as wind effects, wildlife, and moving water reflections must be negligible [32]. Wind can induce faster small ripples that generate tracts on the surface which can be detected by the LSPIV algorithm [40]. Second, there should be no visible surface tracers or ripples that are advected with the flow [33]. Third, the water surface must be clear [33], and no vortices and confluences [41]. In addition, the site must have adequate lighting. Inadequate or changing lighting conditions may cause the algorithms to lose track of surface patterns and may induce undesirable false positive detections due to glare or shade on the water [32]. All these may contradict the true surface flow and impact the accuracy of flow approximation [32].

2.3.2. CHTTC

The CHTTC is located eighty-three kilometers Northeast of Winnipeg City on the Winnipeg River in Seven Sisters Falls, Manitoba and has been an ideal location where researchers from all over the world to conduct and test new developments in the design of hydrokinetic turbines, and open channel water surface velocity measurement in collaboration with the University of Manitoba, as shown in Figure 6. The CHTTC obstruction-free view [41] makes it an ideal location to conduct open channel LSPIV research (Figure 7) and has made this site the preferred location for hydrokinetic turbine placement [26].

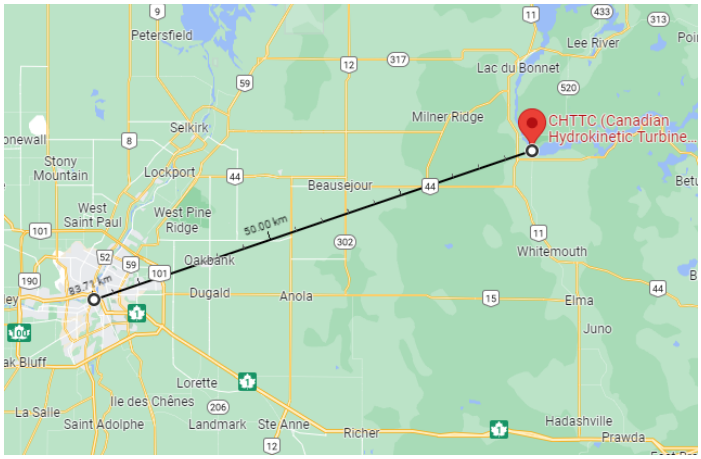

Figure 6: CHTTC location in Manitoba

Figure 7: Clear no obstruction CHTTC view

2.3.3 Favorable weather conditions

Weather conditions play an important role in image velocimetry analysis. Unlike in a laboratory environment, the natural environment can initiate several factors such lighting, wind, rain, snow, and fog that are uncontrollable and greatly influence the accuracy of results. Poor lighting conditions may introduce noise and interference [19], while too much light can introduce glare on the water surface that can cause false color gradients across the AOI [42]. Proper lighting

produces images with a usable set of grey levels that is imperative for LSPIV analysis [43]. In addition, the disparity of lighting can introduce shadows and reflections that are very different from the normal water surface [23]. Free surface reflection is the most common noise usually caused by the Fresnel reflection of sunlight on the water surface (i.e., Sun glitter), causing the image sensor to oversaturate [44] blocking the useful particle signal. See Figure 8. Adding a polarized filter can reduce the reflection but does not eliminate it [23]. Therefore, it is recommended to avoid direct sunlight reflection since there is no known method to remove this type of noise [44].

Figure 8: Sun glitter reflection

Wind can affect both the surface velocity and tracer displacement [23]. In 2019 Pena-Haro et al. concluded that the wind effects on water surface velocity can vary from 3% for wind speeds with an average of 2.3 m/s to 8% if the wind speed averages 10 m/s when the wind opposes the flow direction of the water surface [45]. Thus, wind affects more when the water surface velocity is low, and when its magnitude is significant compared to the flow [42]. Rain (Figure 9A) and snow can affect velocimetry analysis by breaking up the foam patterns [23]. However, the impact of precipitation and snow is not fully understood. But it is known to blur and scatter imagery, causing researchers to disregard data and results when they are present [35] [46]. Fog (Figure 9B) affects velocity results by increasing the surface noise significantly which essentially prevents surface patterns from being traced [42].

Figure 9: (a) Fog and (b) rain noise on water surface

2.3.4 Wind effect correction

Hydro-STIV manual presents a surface velocity correction to correct for wind effects as

$$V_{corr} = V_{mms} - U_{wind} * 0.074 \quad (8)$$

where V_{corr} is the river surface velocity after correction for wind effects, V_{mms} is the measured river surface velocity, U_{wind} is the wind speed measured by an anemometer installed at the site, and 0.074 is the correction coefficient obtained from field observation [47].

2.3.5 UAV image acquisition

Proper image acquisition is essential for accurate water surface velocity. Sufficient water surface texture is a fundamental necessity in LSPIV analysis. That is, the flow must be marked or traced by suitable selected particles [48]. Adding tracers has been an accepted measure for low-flow condition where surface particles or natural tracers may not be sufficient [41]. However, Creutin et al. concluded that seeding densities are not necessary, especially near river banks [49], and experiments on LSPIV tests can be done with natural flow tracers such as water surface ripples without adding artificial tracers [21].

2.3.6 Image orthorectification and transformation

In a field application, it is difficult to image the water surface. The angle formed between the video camera lens and the water surface may present spatial distortions in the images [50] . The transformation algorithm developed by Fujita et al. in 1998 [51] allows for a simplified

transformation approach between two-dimensional Image Plane (Sensor) / screen coordinates (x, y) to the physical coordinates (Figure 10) / object plane (X, Y, Z). The transform equations (10) and (11) are used as a first guess of the mapping relationship [17], and are set using the coordinate data from ground control points (GCP).

$$x = \frac{A_1X + A_2Y + A_3Z + A_4}{C_1X + C_2Y + C_3Z + 1} \tag{10}$$

$$y = \frac{B_1X + B_2Y + B_3Z + B_4}{C_1X + C_2Y + C_3 + 1} \tag{11}$$

where A_1 to C_3 are transform coefficients determined by the least square method using the GCP coordinates. Then, the collinearity equations (12) and (13) express the reciprocal transformation relation between the image and object plane coordinate and are used to determine the final mapping relationships with some trial and error.

$$x - x_0 = -f\left[\frac{a_{11}(X - X_0) + a_{12}(Y - Y_0) + a_{13}(Z - Z_0)}{a_{31}(X - X_0) + a_{32}(Y - Y_0) + a_{33}(Z - Z_0)}\right] \tag{12}$$

$$y - y_0 = -f\left[\frac{a_{21}(X - X_0) + a_{22}(Y - Y_0) + a_{23}(Z - Z_0)}{a_{31}(X - X_0) + a_{32}(Y - Y_0) + a_{33}(Z - Z_0)}\right] \tag{13}$$

where, (X_0, Y_0, Z_0) are the physical coordinates of the camera, (x_0, y_0) are the principal coordinates of the screen, f is the focal length, and a_{ij} are coefficients related to the camera angle.

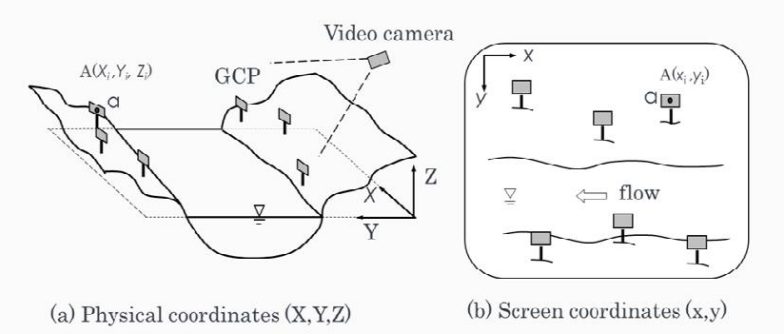

Figure 10: Ground control point arrangement and screen coordinates [17]

2.3.7 Nadir image

To speed up georeferencing by skipping the use of ground control coordinates, a Nadir image is used. Nadir image is an aerial photo taken with a camera or drone (UAV) facing directly beneath the camera or pointing directly downwards, as shown in Figure 11 at a -90-degree angle towards the ground [52]. Figure 11 also shows how a Nadir image offers no lens distortion using a checkboard pattern and differs from oblique images that will require calibration due to lens distortion. Therefore, a Nadir video taken from an off-shelf commercially and publicly available digital camera and even a low-cost drone with a mounted digital camera can be used to estimate water surface velocity using Digital Particle Image Velocimetry (DPIV) [53].

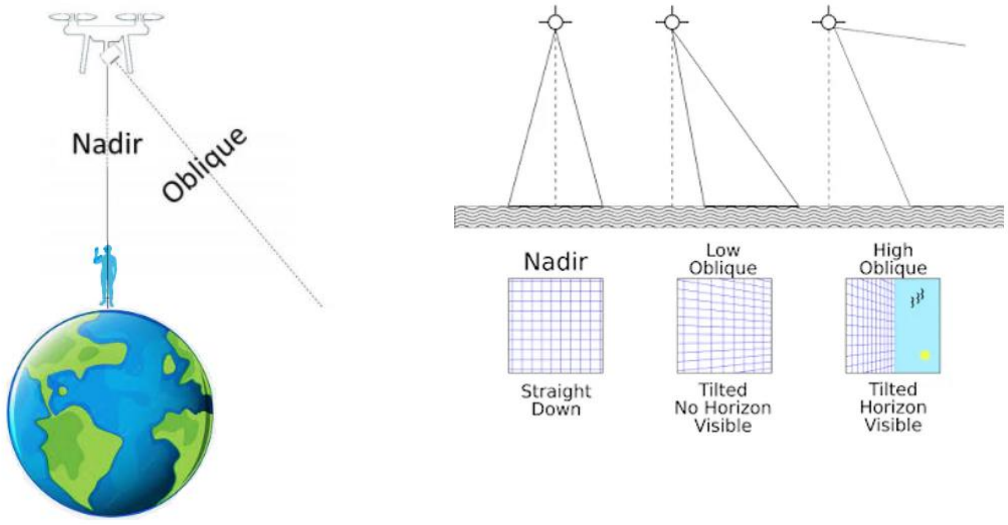

Figure 11: Nadir image from reference [52]

By using a Nadir image, rectification of the image is not necessary since the drone's x, y position is equal to the x, y position of the center of the image [53]. In addition, lens distortion can be ignored since it does not introduce significant errors in a drone video [54].

2.3.8 Ground sampling distance

The Ground Sampling Distance (GSD) is the distance between the center points of two adjacent pixels as measured on the ground. GSD is essentially the size of one pixel on the ground. GSD is illustrated in Figure 12.

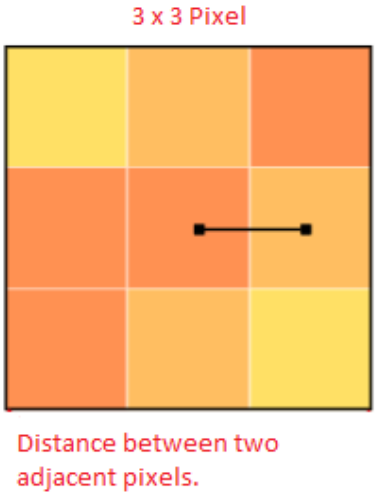

Figure 12: Pixel image GSD

Knowing the GSD before starting the image acquisition is important. This is because free-surface texture can be determined by adjusting the flight height of the drone, allowing greater detail on the area being reconstructed (e.g., flying the drone in low altitude). To calculate for GSD, we draw two similar triangles T_1 and T_2, as shown in Figure 13.

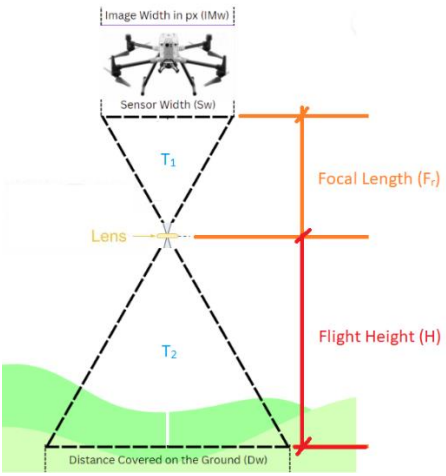

Figure 13: GSD calculation

T_1 is formed from the drone image sensor width to the lens, and T_2 is formed from the lens to the ground distance width. From geometry, we can write equation 14.

$$\frac{Ground\ Distance\ Width\ (D_w)}{Sensor\ Width\ (S_w)} = \frac{Flight\ Height\ (H)}{Focal\ Length\ (F_r)} \quad (14)$$

However, we know that the ground distance (D_w) is the GSD multiplied by the number of pixels of Image width (I_w) (equation 15).

$$D_w = GSD\ x\ I_w \quad (15)$$

Substituting equation 15 to 14, and re-writing equation 14, we have GSD as:

$$GSD = \frac{S_w\ x\ H}{F_r\ x\ I_w} \quad (16)$$

where H is the height above the surface in meters, F_r is the focal length of the camera in millimeters, S_w is the sensor width in millimeters, and I_w is the image width in pixels. By knowing the GSD, the length of one pixel can be used to assign real-world coordinates to all pixels [53].

2.3.9 DJI Phantom III professional GSD

From Table 4, the width of the frame is 2160 (I_w) and the sensor size is 2.3" (S_w), the drone was flown at a height of 80 m (H), and the focal length (F_r) is 9 mm (taken from the image property details). The width of the sensor from Table 4 is 6.16 mm. From equation 14 we have:

$$GSD_{DJI} = \frac{6.16\ x\ 80}{9\ x\ 2160}$$

$$GSD_{DJI} = 0.0253\ m$$

Since this was a video file with a frame rate of 30 fps, we have:

$$GSD_{DJI} = 0.0253\ x\ 30$$

$$GSD_{DJI} = 0.759\ m$$

This means that at 30 fps, the velocity equivalent of 1 pixel movement between frames is 0.759 m/s for the DJI Phantom III professional drone.

Table 4: Sensor image area dimensions

Sensor "Type"	Imaging Area Dimensions (mm)		
	Diagonal	Width	Height
1/6"	2.7	2.46	1.8
1/4"	4.5	3.6	2.7
1/3.6"	5	4	3
1/3.2"	5.68	4.54	3.42
1/3"	6	4.8	3.6
1/2.7"	6.59	5.37	4.29
1/2.5"	7.18	5.76	4.29
1/2.4"	7.66	5.92	4.57
1/2.3"	7.7	6.16	4.62
1/2.33"	7.8	6.13	4.6
1/2"	8	6.4	4.8
1/1.8"	8.93	7.18	5.32
1/1.75"	9.23	7.38	5.54
1/1.7"	9.5	7.6	5.7
1/1.6"	10.07	8.08	6.01
2/3"	11.07	8.8	6.6
1"	16	12.8	9.6
4/3"	22.5	18	13.5
APS-C	Sony	21.5	14.4
	Canon	22.2	14.8
	Nikon	23.7	15.7
	Canon	28.7	19.1
35 mm	43.3	36	24

2.3.10 Image stabilization

Several tests have been conducted on how wind affects drone stability and how it affects velocity measurements. Stabilization is only necessary when the camera is not fixed, vibrations are present, or when there is high wind turbulence and gustiness [42] [53]. Using un-stabilized images when conditions require image stabilization can contribute to errors, and a re-analysis must be made since these errors can affect data by 20-30% [55].

However, current modern drones are equipped with gimbals that act as an image stabilization system that maintains its orientation regardless of drone movement [53]. These newer drones

have been tested with a wide range of windspeeds at an elevation of 120 m, as shown in Figure 14. The results gave an average of less than one pixel GSD, or 0.07 to a maximum of 0.15 m/s. The tests also concluded that there was no notable difference between drone movement and wind speed [53].

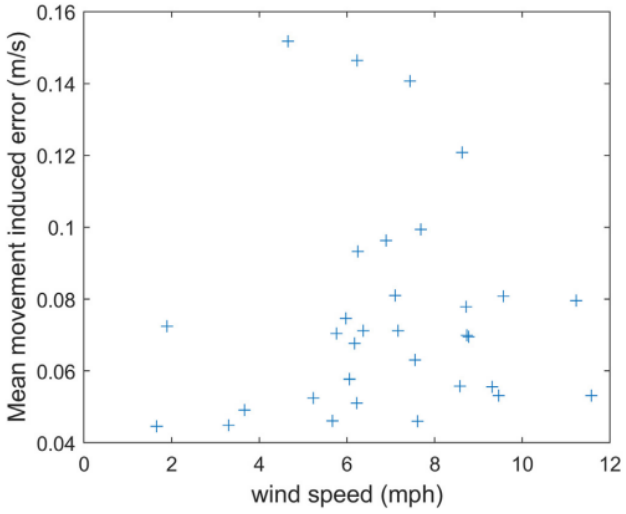

Figure 14: Drone stability against wind speed [53]

2.3.11 Selecting region of interest (masking)

Masking or selecting a region of interest (ROI) is an important step in LSPIV pre- processing. Stationary objects and surfaces usually appear in PIV images, and these contribute to the cross-correlation (CC) function and introduce errors in the vectors [56]. CC is the most sensitive part of DPIV [39]. It is a correspondence technique commonly used in low-density image mode and is computed by comparing the interrogation of a small region or area on the stream surface of the first and second images [48] (Figure 15). Essentially, CC is a numerical analysis that compares IA A and B and finds a pattern between them [39]. When comparing regions A and B, the size of the ROI and the IA are user-defined [41].

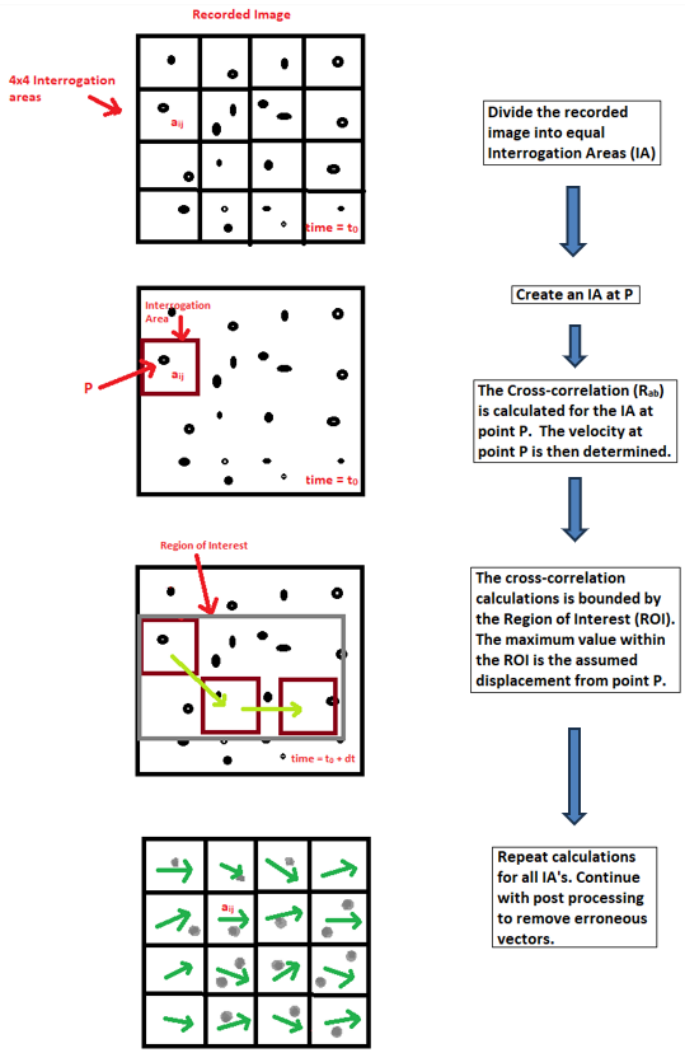

Figure 15: Typical CC flow chart

A CC algorithm is applied between successive images to match flow patterns [48], and the highest value in the correlation coefficient is used as the direct estimate of the particle image displacement [57]. CC is the preferred standard for image processing software [41], and is given by [50] [51]:

$$R_{ab} = \frac{\sum_{i=1}^{MX}\sum_{j=1}^{MY}\{(a_{ij} - \overline{a}_{ij})\}}{\left\{\sum_{i=1}^{MX}\sum_{j=1}^{MY}(a_{ij} - \overline{a}_{ij})^2 \sum_{i=1}^{MX}\sum_{j=1}^{MY}(b_{ij} - \overline{b}_{ij})\right\}^{1/2}} \quad (17)$$

where R_{ab} is the CC coefficient, and MX and MY are the size of the interrogation areas in each of the recorded images. Variables a_{ij} and b_{ij} are the distributions of the gray-level intensities in the two interrogation areas separated by the time interval dt. The overbar is the mean value of the intensity for the interrogation area. However, using CC in a normal PIV interrogation area or window will have several thousand pixels and require one million multiplications and summations which require a substantial computational effort [57]. Reducing the interrogation area window size is one way to reduce computation size, but it must still be small enough to preserve the spatial scale of interest [41]. Thus, a less computationally taxing method is needed.

An alternative method to the computation intensive CC is the use of the Fast Fourier Transform (FFT). Using FFT simplifies and significantly speeds up the CC process. The process can be brought down to a complex-conjugate multiplication of each corresponding pair of Fourier coefficients, rather than performing the sum of all the elements of the sampled region for each element as in equation 17 [58]. In addition, compared to $O[N^4]$ for the direct computation of the two-dimensional correlation, the process is simplified to $O[N^2 \log_2 N]$ [57]. The CC using FFT is outlined in Figure 16.

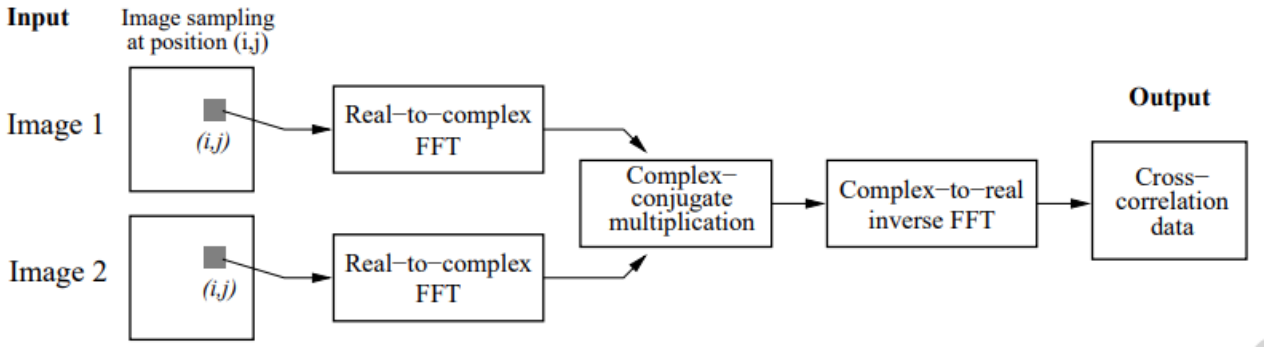

Figure 16: Implementation of CC using fast Fourier transform [57]

There are two dominant masking methods: Dynamic for moving objects and Static for stationary. For moving objects, masking is difficult and time consuming. Thus, dynamic masking where thousands of images can be acquired is simply not practical and very complicated [56]. This thesis will focus on static masking as this is straightforward, and any reference to dynamic masking technique is left out.

2.3.12 Image enhancement

Often, images are captured during sub-optimal conditions such as poor or excessive lighting, shadows, obstacles, and many other scenarios that can introduce image noise. This happens more in practical applications and can affect the accuracy of the PIV data results [19]. Therefore, image enhancement is necessary to reduce image noise and create a more coherent and evenly distributed image texture [19] that will allow the PIV software to better track particle movement on the water surface.

Several algorithms are available; the three common image enhancing algorithms that will be discussed in this section are Contrast-limited adaptive histogram equalization (CLAHE), high-pass filter, and intensity capping.

The first algorithm CLAHE is an image enhancing method that limits the over-amplification of contrast done by histogram equalization (HE) depending on the user specified set limit. By limiting the contrast over-amplification enhancements done by HE, desired results can be achieved [59]. Figure 17 shows how CLAHE and HE filter process the original image.

Figure 17: CLAHE image transformation [60]

The second algorithm used for image enhancement is using a high-pass filter or image sharpening. Essentially, the high-pass filter inhibits the low frequency information by preserving the high frequency details in an image [39] [61]. Thus, when the high-pass filter is activated, it causes small and faint details to be exaggerated. The final technique is intensity

capping. This filter rectifies a common source of error in PIV where bias is created by bright specks characterized by grayscale intensities much higher than the mean intensity that appears in the IA's resulting from non-uniform flow. By adding a user-specified upper limit to the greyscale intensity, any pixel whose intensity goes over this limit is replaced by the user-specified limit which in turn reduces the bright spots [39][62]. So, unlike the CLAHE algorithm where the whole image is amplified including the background noise creating errors; intensive capping only changes particles that go over the set limit, thus avoiding noise amplification [39] [62], and is then less computationally taxing than CLAHE [62]. Therefore, using the intensity capping filter increases the number of valid vectors and displacement errors are reduced [62]. Figure 18 shows the summary of how the three (3) filters process an image in CHTTC during drone capture.

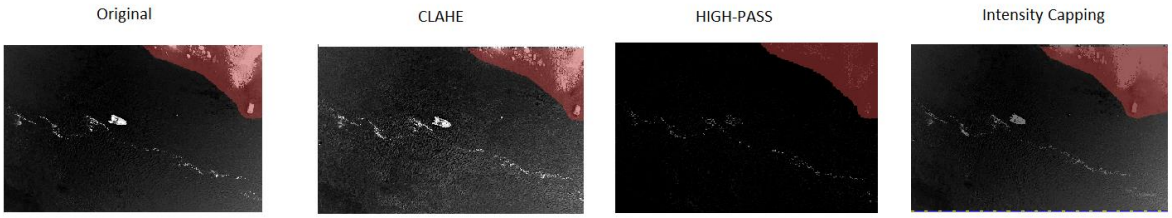

Figure 18: Image enhancing technique effects summary

2.3.13 Calculating velocity vectors

Translating pixel displacement information into real world numbers (such as m/s) is crucial to understanding water surface velocity displacement data. The first step is to find a reference distance within the image such as having GCP, and then divide the displacements by the inter-frame time [63]. The timeframe or time step TS is

$$TS = \frac{1}{FR}\ x\ 1000 \tag{18}$$

where TS is the time step in milli-second, and FR is the frame rate.

2.3.14 Vector validation

Frequently, resultant vectors in automated PIV will include several erroneous vectors [63] that will require data validation. Hence, vector validation is necessary to create accurate and reliable data [64]. Erroneous vectors are often seen as vectors that "stand-out" since they read much higher and often different than the surrounding vectors. Thus, it is easy to note these vectors [63].

In this process, erroneous vectors (vectors that are too far or "outliers" [39] [65]) that are caused by a number of factors such as a disparity in seeding particles, or little to over illumination of an image are filtered and removed semi-automatically by differentiating or by selecting an acceptable lower and upper limit [39]. The lower and upper thresholds are represented by equations 19 and 20:

$$t_{lower} = \bar{u} - n * \sigma_u \quad (19)$$

$$t_{upper} = \bar{u} + n * \sigma_u \quad (20)$$

where u is the mean velocity, $\boldsymbol{\sigma}_u$ is the standard deviation of u, and n is the accuracy of the filter and is user defined.

After the erroneous vectors are removed, they are replaced by vectors that are very close to the local flow velocity. These new vectors are usually found by interpolated data [64] [63] shown in Figure 19. The most common method is using a 2-D interpolation. However, using simple linear or polynomial interpolation is the straightforward and uncomplicated way to yield appropriate results [63]. To yield the most accurate results, a spline interpolation must be used [39] [63]. Unlike regular interpolation, spline interpolation leaves the native adjoining data untouched and finds the removed data by "the most fluent line or plane" [63]. In PIVlab, it uses a boundary solver function in MATLAB' called "inpaint_nans" [39]. This function produces interpolated data that is smooth over a large area of missing data and then averages the boundary velocities to prevent overshooting [39]. After the data is interpolated, data smoothing is applied to remove residual noise in the vectors. There are several methods that have been proposed for data smoothing. A data convolution with 2·2 or 3·3 kernels with equal weight or

by median filtering has been proposed by Raffael et al. [57]. Finally, smoothing DPIV by applying the penalized least square method is proposed by D. Garcia [66]. The final method by Garcia is the smoothing algorithm that PIVlab applies.

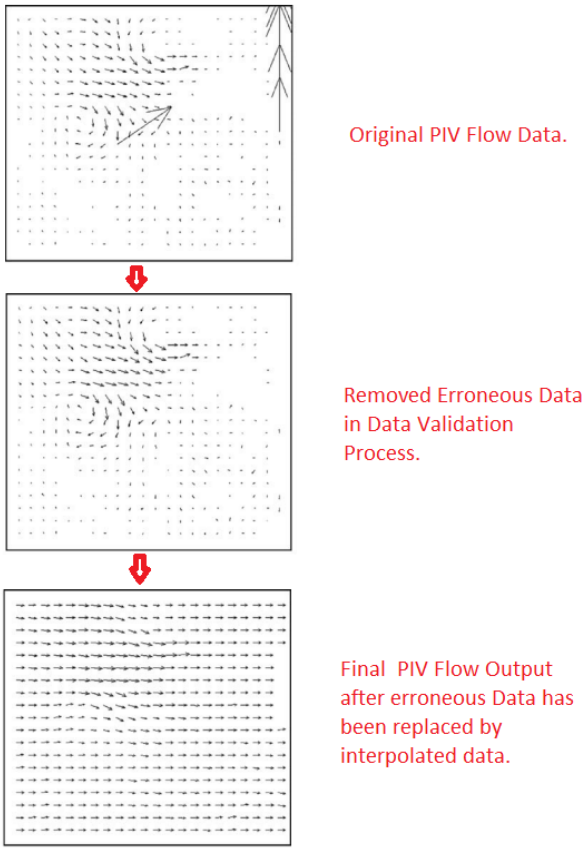

Figure 19: PIV data validation process

2.4 LSPIV studies

Table 5 shows STIV and LSPIV studies that have been undertaken mainly in rivers. Some of the main conclusions are also listed form each study. From these studies one can note that no LSPIV studies have been applied to measure energetic river site to locate RHKT.

Table 5: Field studies LSPIV

Author	Imaging technique	Site type	Acquisition method	Verification method	Results
Zhang et al. [44]	STIV	Laboratory water tunnel	Photogrammetry	Propeller current meter	The proposed STIV is superior to propeller current meters and surface velocity radars in shallow free-surface velocity measurements.
Fujita et al. [17]	STIV	River	River Monitoring Camera	ADCP	Results show that STIV error os small enough and can be considered an accurate velocity measurement.
Han et al. [36]	STIV	River	UAV	Propeller flow meter	Results show that STIV error os small enough and can be considered an accurate velocity measurement.
Zhao et al. [19]	STIV	River	Camera in river bank	Impeller style current meter	STIV with denoising allows surface velocity measurement errors to be within 6%.
Fairley et al. [53]	LSPIV	Ocean	Drone	ADCP	The Drone video provided suitable surface velocities under favorable environmental conditions.
Masafu et al. [65]	LSPIV	River	Drone	ADCP	Results show that LSPIV results are on par with ADCP results.
Koutalakis et al. [28]	LSPIV, STIV	River	UAV	Not Applicable (NA)	Results show that PIV and STIV softwares had near identical results. However, the authors had no way to verify the water surface measurements.
Coz et al. [21]	LSPIV	River	Fixed Camera	ADCP	LSPIV results were in agreement with ADCP and deviated less than 20% from ADCP results in good image conditions. Under poor conditions, deviation increased to 30-80%.

Chapter 3: Experimental procedures

This research aims to evaluate the feasibility and accuracy of using DPIV to evaluate the surface river velocity to estimate hydrokinetic resources. To do this, we fly a drone over the CHTTC test site to collect videos of the river surface, use two DPIV simulation software called PIVlab and OpenPIV to extract velocity data, and utilize an ADV to compare and validate the simulated results. In addition, laboratory measurements then completes the study.

3.1 Difficulties encountered working in open channel

When working with energetic rivers, multiple factors are beyond the control of researchers. The first issue is the wind. Conventional river surface velocity measurement devices such as acoustic instruments are less susceptible to wind effects since they are deployed under water. Here the DPIV method uses natural water surface ripples to analyze and calculate surface velocity. Since the surface texture of water can be affected by wind, finding the limit when the wind impact is minimal is an important consideration.

Another issue is the ADV itself used to validate the method. D'Auteuil noted in his research that ADV exerts a drag force of 100 N or 10 kilograms (kg) [26]. His calculations were based on flow velocities recorded at the CHTTC which varies from 1.6 to 3 m/s. The drag force is based on [27]:

$$F_D = \frac{1}{2} C_D \rho U^2 A \tag{21}$$

where C_D is the drag coefficient of the body experiencing the drag, and A is the cross-sectional area that is exposed to the flow. D'Auteuil concluded that the weight of the ADV, the amount of time the experiment is conducted, and the vortex shedding that takes place creating vibration problems will exert more force on the ADV mounting which is already experiencing a significant drag force by itself.

Finally, concerns that are innate when working on a river such as:

- Experiencing hypothermia due to the cold weather.

- Hazards that can cause personnel to trip and fall into the flowing river.
- The boat can accidentally hit shallow areas when traversing causing damage and injuries.
- Transporting sensitive, bulky, and heavy equipment that can be damaged due to the vibrations and impacts caused by uneven terrain.
- Mounting equipment may fail during experiments due to the large forces experienced when underwater.
- Ropes that can get entangled and cause injuries.
- Finally, personnel fatigue when working long hours.

3.2 UAV flight

The objective of flying a UAV / Drone is to hover over the AOI at the site and collect video data. The drone being used in this study is a DJI Phantom III Professional. Specifications of this UAV are listed in Table 6. Figure 20 shows the DJI Phantom III Professional with accessories.

Table 6: DJI Phantom specifications [67]

DJI Phantom III Professional Specifications				
Drone Specifications			**Camera Specifications**	
Take off Weight	1280 g		Sensor	½.3" CMOS, 12.4M (Effective)
Diagonal Size (w/o Propellers)	350mm		Lens	FOV 94˚ 20mm (35mm equivalent) F/2.8
Max Flight Time	23 mins		ISO Video Range	100-3200
Satellite Positioning	GPS		Video Resolution	4096 x 2160 (4K)
Hover Accuracy Range	Vertical: +/- 0.5m Horizontal: +/- 1.5M		Format	MP4, MOV (H.264, MPEG-4 AVC)
Max WiFi Transmission Range	FCC: 1000m CE: 500m		Stabilization	3-axis (pitch, roll, yaw)

Figure 20: DJI Phantom Professional III

A drone certified pilot flies the drone at an altitude of 80 m and the maximum permissible flight height in Manitoba is 122 m. While flying the drone, it was always in sight, and away from bystanders, airports, and heliports, thereby fully abiding under Manitoba, Canada legal requirements [68]. Video frame size is set at 4k which is 4096 x 2160 pixels (px), and 30 fps is considered sufficient in capturing surface velocities for LSPIV analysis in both hydraulic and hydrologic applications [32]. The drone camera has an automatic stabilization system with a three-axis gimbal, as shown in Table 2 DJI specifications, that compensates for pitch, roll, and yaw allowing steady smooth camera footage while moving in flight.

To enable georeferencing without having to put ground control points, Nadir imagery was implemented throughout the process of filming the river surface by focusing the camera at -90^{o} or downward-looking, as shown in Figure 11.

For lens distortion correction, no correction has been applied. The DJI Phantom Pro III's 94^{o} Field Of View (FOV) has been tested by Streber et al. and they concluded that the UAV's FOV provides distortion free images and videos [54].

Finally, the weather conditions during the UAV flight had negligible winds, and thus, it was assumed that the drone remained stationary during the video recording process.

3.3 ADV site

The goal of this section is to present how to take ADV measurements at the CHTTC site and establish base velocity measurements near the water surface. ADV's provide accurate measurements in challenging areas where conventional techniques will provide inaccurate results, such as unsteady, bi-directional, or wind-affected flows [69]. Measurements are performed using a Nortek Vector ADV to provide river surface velocity readings to compare to LSPIV. Figure 21 shows the specifications and a Nortek ADV picture.

Nortek Vector Current Meter Specifications	
General:	
Weight	5 kg. (in air), 1.5kg (in water)
Length Diameter	550mm with batteries, 450mm without 75mm.
DC Input	9-18VDC.
Max Consumption at 64 Hz. Typical Consumption at 4 Hz.	1.5 W 0.6 - 1.0 W
Temp Range	-4 to +40 degree Celsius
Compass Max Tilt	30 degrees
Tilt (Liquid level)	0.2 degrees / 0.1 degrees for tilt < 20 degrees
Pressure	0-20m (standard)
I/O	RS-232 or RS-422
Baud Rate	300 - 115200
Water Velocity Measurement	0.01; 0.1; 0.3; 1; 2; 4; 7 m/s (software selectable)
Sampling Rate	1-64Hz
Acoustic Frequency	6 MHz
Resolution	0.45dB

Figure 21: (a) Nortek ADV specifications, and (b) picture of instrument

The ADV is mounted on a boat that has been modified to carry the depth-arm, which is a specially fabricated mounting to house the ADV. The depth-arm then lowers the ADV under water at a depth of 1 m and a locking mechanism ensures that the ADV remains stationary under water. Figure 22 details the specialized boat.

Figure 22: Specialized boat with Nortek ADV

Once underwater, the ADV transmits acoustic pulses known as water pings [69] at a constant 10 MHz frequency that covers 3 to 15 mm control volume from the transmitter shown in Figure 23, and the receiver listens to the reflected echo and is recorded in each of the acoustic receiver elements.

Figure 23: ADV receiver and transmitter locations

The change in frequency between the transmitted and received echoes is called the Doppler Effect. This effect is what is used to measure the relative velocity between the suspended particles and the ADV. The Doppler Effect can be calculated as [70].

$$F_D = 2F_S\left(\frac{V}{c}\right) \tag{22}$$

where F_D is the change in received frequency, F_S is the frequency of the transmitted sound, V is the relative velocity between transmitter and receiver, and *c* is the speed of sound. Finally, a real-time differential global positioning system provides boat position, ensuring that the boat is stationary at the current position without being anchored as shown in Figure 21, and the ADV collects the water surface velocity data. The collected data from the ADV is sent through a Panasonic Toughbook laptop personal computer (PC) with a Core i5 Windows 7 and product model CF-31, as shown in Figure 24.

Figure 24: Panasonic Toughbook CF-31 used for field work

The PC converts the data downloaded from the ADV with a Nortek Vector software version 1.39.39 to three file formats as shown in Figure 25: velocity data (*.dat), burst header data (*.vhd), and sensor data (*.sen). These files can all be opened with a notepad. Figure 25 shows how to read the data in notepad. For example, if we want to find the velocity in the X direction, we open the "*.dat" file with notepad, and look at the 3rd column.

Velocity data (.dat)

Col.	Type	Unit
1	Burst counter	
2	Ensemble counter (0–65535)	
3	Velocity (beam 1, x or east)	m/s
4	Velocity (beam 1, y or north)	m/s
5	Velocity (beam 1, z or up)	m/s
6	Signal strength (beam 1)	counts
7	Signal strength (beam 2)	counts
8	Signal strength (beam 3)	counts
9	SNR (beam 1)	dB
10	SNR (beam 2)	dB
11	SNR (beam 3)	dB
12	Correlation (beam 1)	%
13	Correlation (beam 2)	%
14	Correlation (beam 3)	%
15	Pressure	m
16	Analogue input 1	
17	Analogue input 2	
18	Checksum	1= failed, 0=OK

Burst header data (.vhd)

Col.	Type	Unit
1	Month	
2	Day	
3	Year	
4	Hour	
5	Minute	
6	Second	
7	No. of velocity samples	
8	Noise amplitudes (beam 1)	counts
9	Noise amplitudes (beam 2)	counts
10	Noise amplitudes (beam 3)	counts
11	Noise correlation (beam 1)	%
12	Noise correlation (beam 2)	%
13	Noise correlation (beam 3)	%

Sensors data (.sen)

Col	Type	Unit	Remarks
1	Month		
2	Day		
3	Year		
4	Hour		
5	Minute		
6	Second		
7	Error code		Explained in a separate table
8	Status code		Explained in a separate table
9	Battery	V	
10	Sound speed	m/s	
11	Heading	°	
12	Pitch	°	
13	Roll	°	
14	Temperature	°C	
15	Analogue input		
16	Checksum		1= failed, 0=OK

Figure 25: Nortek Vector output file types

A summary of the ADV site procedure is shown in Figure 26.

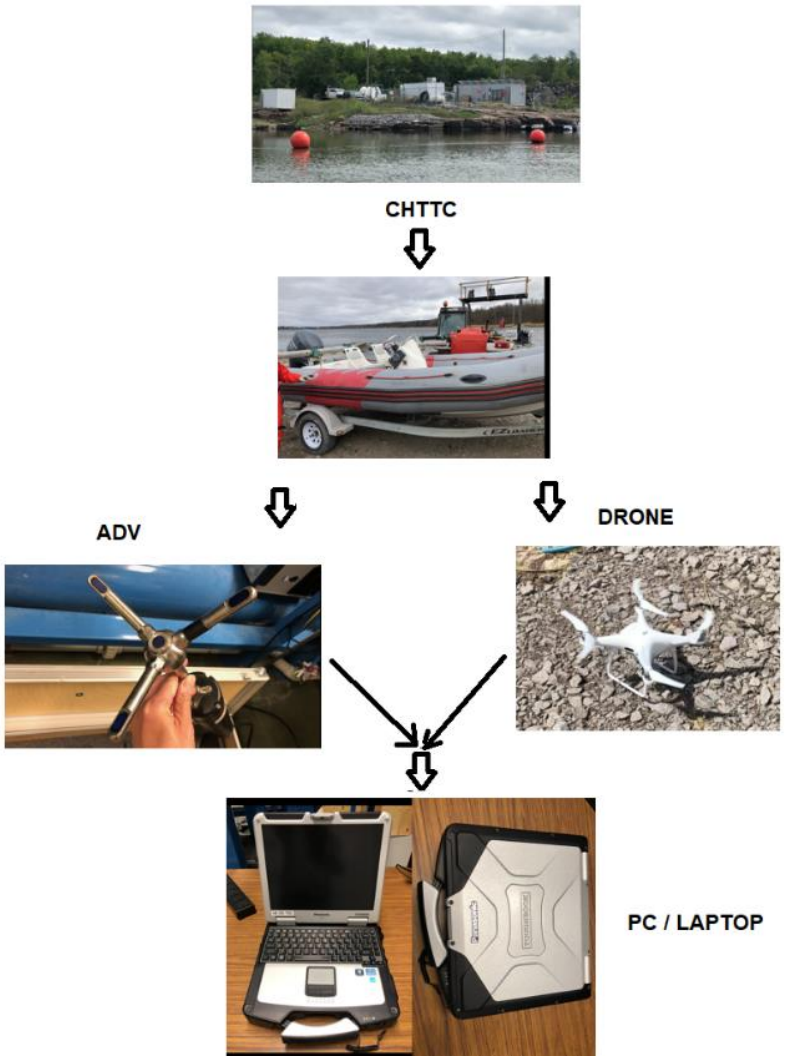

Figure 26: ADV site procedure summary for validation also showing drone video capture to perform.

3.4 Laboratory

A water tunnel is also used to provide water flow in a controlled environment. By using a water tunnel, we can create consistent water surface velocity devoid of wind effects and other natural phenomena that can affect the water surface ripples and introduce errors in the data analysis. The tunnel is in the Engineering Faculty at the University of Manitoba. Figure 27 shows the water tunnel. The equipment has a maximum permissible water height of 60 cm and is coupled with a single stage axial flow propeller pump with 30 hp, 60 Hz, three-phase Toshiba motor running at 1,800 rpm delivering 362 l/s. To control the water flow speed, a variable speed control inverter increases or decreases the input frequency power fed into the motor, thereby increasing or reducing the motor speed, which then increases or decreases the water velocity inside the water tunnel. The inverter shown in Figure 27.

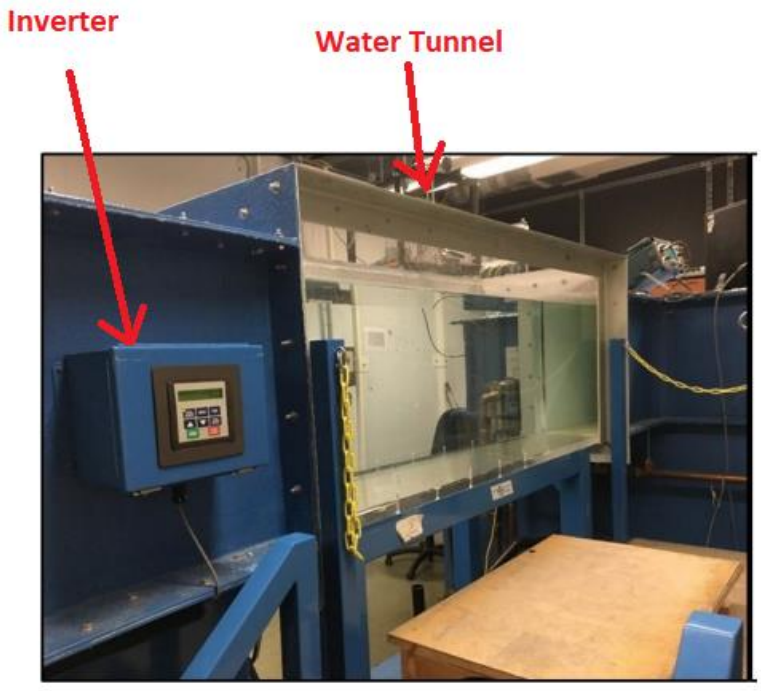

Figure 27: Water tunnel used in the experiment

To ensure that the water speed velocity is accurate, the water tunnel is calibrated with an ADV. In addition, the tunnel was left empty except for the water inside, ensuring unobstructed flow,

and no wind effects. The calibrated tunnel inverter frequencies versus water speed are shown in Table 7.

Table 7: Calibrated water tunnel velocity chart

Velocity (m/s)	Frequency (Hz)
0	0
0.1	5.7
0.2	11.3
0.3	17
0.4	22.6
0.5	28.3
0.6	33.9
0.7	39.6
0.8	45.2
0.9	50.9
1	56.5

Graphing Table 7, we observe that the water velocity flow versus the motor power input frequency follows a linear pattern. The linear behavior of the water tunnel speed with respect to the power input can be attributed to the water tunnel having a clear and unimpeded flow, which is shown in Figure 28.

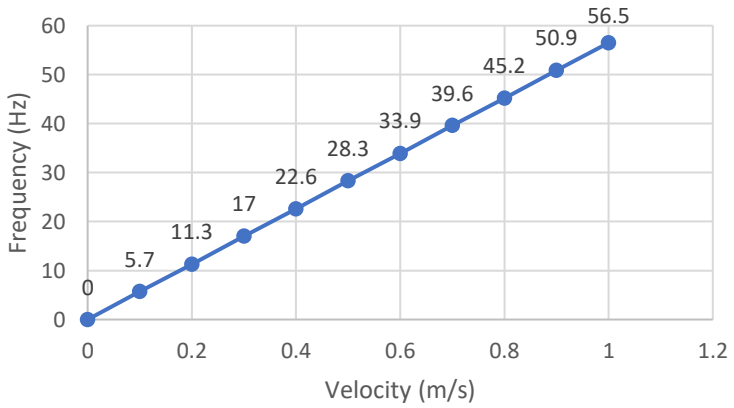

Figure 28: Calibrated water tunnel velocity to frequency chart

Finally, Figure 29 summarizes the laboratory flow procedure.

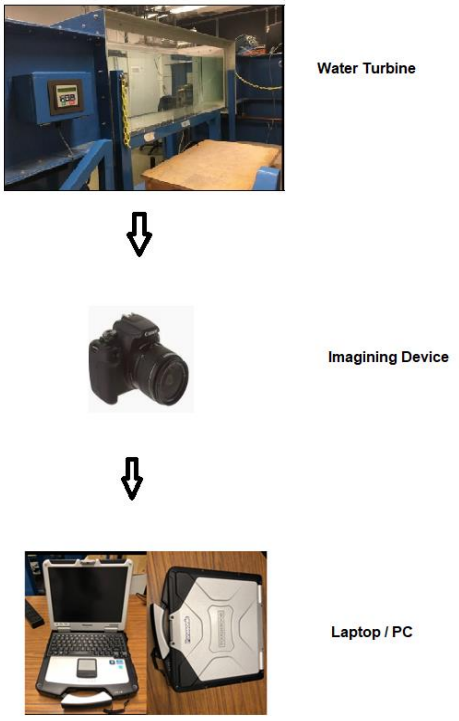

Figure 29: Laboratory flow procedure

3.5 Simulation

Simulation software used in this section will be PIVlab and OpenPIV:

- PIVlab is an open-source software that was developed by Thielicke et al. from a MATLAB environment with a user-friendly Graphical User Interface (GUI) for PIV analysis but can be used for LSPIV applications [22].
- OpenPIV is also an open-source software. The software version used in this thesis was the first version that was programmed solely with Python and did not have a GUI.

3.5.1 PIVlab

PIVlab simulation is gaining popularity among researchers for natural river flow monitoring [71]. The PIV simulations includes pre-processing the images by enhancing the images and selecting the ROI. After pre-processing, the images are post-processed by calibrating and vector validating.

Before PIVlab can process and simulate images, it needs to import files either in video or image files. Before importing, the videos are reviewed to identify sequences that are within the AOI. Once these sequences are found, the video is trimmed to include those sequences, and then imported to PIVlab for pre-processing.

3.5.1.1 PIVlab pre-processing

The first step in pre-processing is to select the ROI and "masking" within the image frame. This is the area where the surface velocity needs to be analyzed, and the masked area is the area that will be excluded from the PIVlab analysis. Figure 30 shows the blue rectangular box which is the ROI, and the masked area in red.

Figure 30: Selection of region of interest

PIVlab has several pre-processing options available. However, it does not have an option to orthorectify images caused by lens distortion when filming from oblique angles. Therefore, imported images must be captured at nadir.

If the image was captured in poor weather conditions, PIVlab offers three image-enhancing filters that will magnify image details for better PIV processing. These filters are CLAHE, high-pass, and intensity capping.

For the site experiment, CLAHE is used to enhance images by limiting extreme contrasts. Since our research is conducted on a good weather, the images were detailed enough not to require additional image processing other than CLAHE as shown in Figure 31.

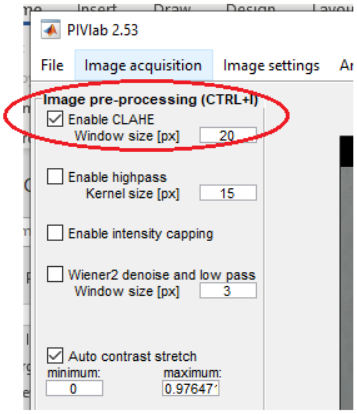

Figure 31: CLAHE image enhancement option

The next step is to choose how the software will calculate cross-correlation. PIVlab offers two options here; Direct Cross-Correlation (DCC) and Fast Fourier Transform cross-correlation (FFT-CC) with multiple passes. Both algorithms are based on the cross-correlation of small interrogation areas (IA's) of image pairs [65] [71]. The first method, DCC calculates the correlation matrix between corresponding IA's in the spatial domain [39] [71]. These paired IA's can be of different sizes. DCC can be best described as "moving the images over one another for best match" [63]. The second method, the FFT-CC is calculated in the frequency domain [71]. Here the paired IA's are of identical sizes. Therefore, every particle movement creates some information loss [39]. This loss can, however, be mitigated by running several particle displacement passes on the same dataset [72] . Both methods have their advantages and disadvantages. DCC is more accurate, but slower because it is more computer-intensive, while FFT-CC is less accurate but faster [72] [73].

This thesis chose the use of FFT-CC to evaluate the cross-correlation between images since it is faster, less computer resource intensive, and yields accurate results by being able to utilize several passes on the dataset. Figure 32 shows the FFT-CC selection.

Since FFT-CC is selected, it is necessary to enable several passes on the dataset to improve accuracy. The width of the IA's used for each pass has been recommended by the developers of PIVlab, and subsequently used by Pumo et al. [71]. Essentially, the width of subsequent IA's is half of the previous pass. The first pass was set to 256 x 128px, the second pass 128 x 64px, the third pass 64 x 32px and finally 32 x 16px all with 50% overlap. Figure 32 shows the resulting IA. By allowing areas to overlap, additional data is made available at the borders and corners of each IA, which is used to determine the displacement of every IA by using bilinear interpolation [39].

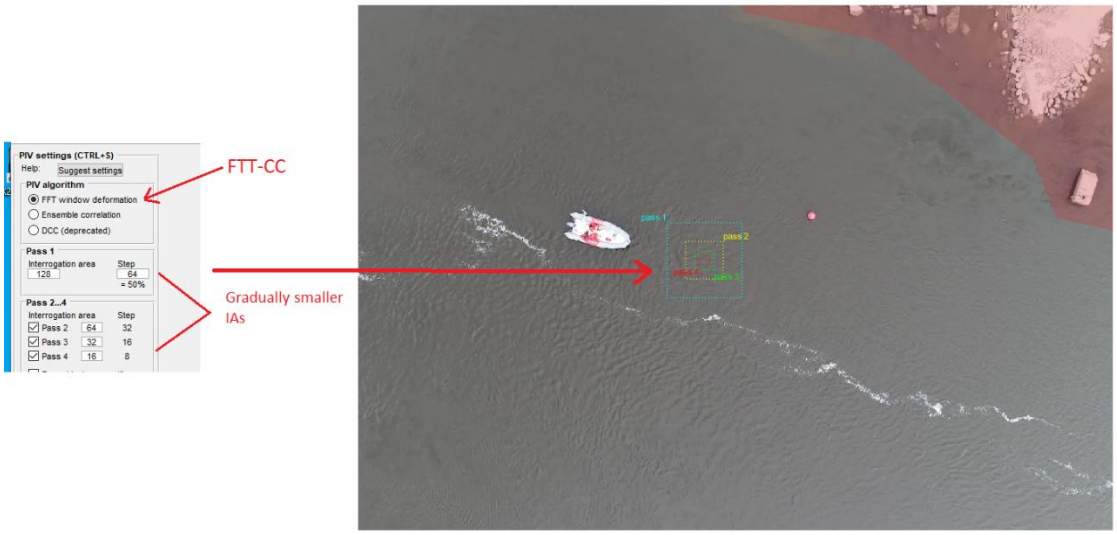

Figure 32: FFT and interrogation area set-up

3.5.1.2 PIVlab post-processing

After the images are processed they then need to be post-processed. Post-processing is an important step since it allows for vectors in pixels to be converted into real-world numbers such as surface velocity in m/s via velocity vector calibration. In addition, post-processing also validates and removes erroneous vectors replacing them with interpolated vectors to improve accuracy.

3.5.1.2.1 PIVlab velocity vector calibration

Vector calibration is a crucial step in PIVlab. It allows us to transform the velocity displacement of pixels per frame into actual surface velocity in m/s. There are two ways to do this in PIVlab. The first method is to choose a reference image, and the second is to select a reference distance. Since we do not have a reference image, but we have a reference distance from the picture, calibration of surface velocity is done through the reference distance method. The reference distance is georeferencing the velocity vectors by specifying a known real distance in the image that PIVlab uses to calculate the surface particle velocity. In Figure 33, two known reference distances are the boats' width and red foam float, both measuring 2,000 mm.

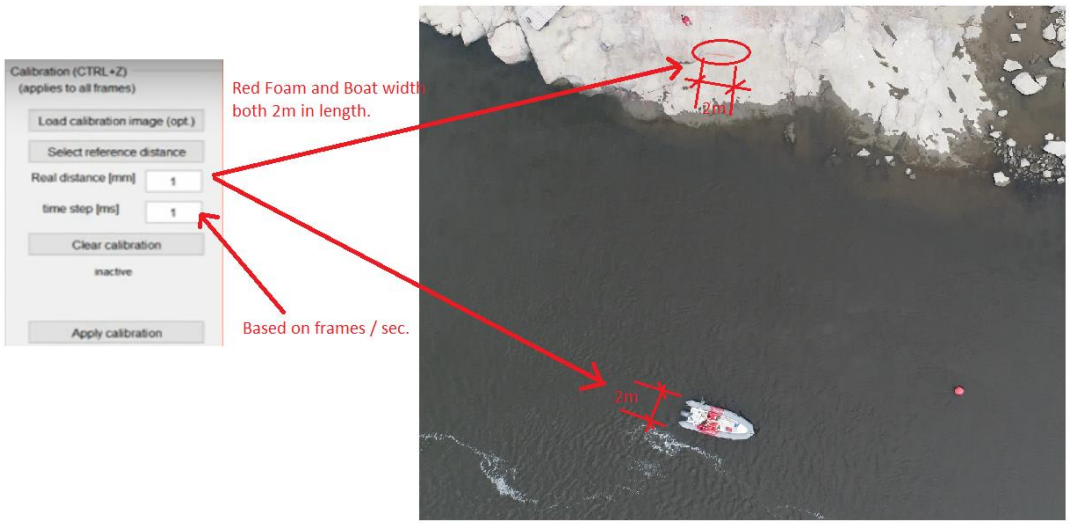

Figure 33: PIVlab calibration

After specifying the reference distance, we specify the time step in ms. The time step is based on the set video recording which can be specified or can be calculated from the video metadata inside the video properties in the details tab. Figure 34 shows the location of the video frame rate found inside the file metadata.

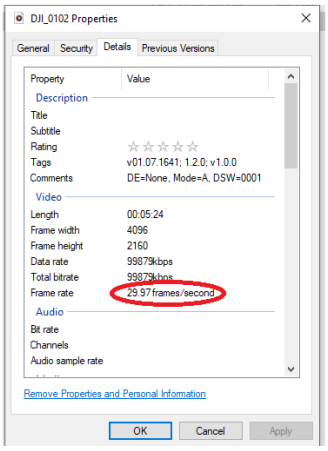

Figure 34: Video property metadata

Since our video frame rate is 29.97 fps from equation 18, we have:

$$TS = \frac{1}{FR}\ x\ 1000$$

$$TS = \frac{1}{29.97}\ x\ 1000$$

$$TS = 33.37\ ms$$

Therefore, the TS for our simulation is 33.37 ms. We can input the resulting TS in PIVlab shown in Figure 33.

3.5.1.2.2 PIVlab data validation

After the pixels have been transformed into real-world velocity displacements such as meters per second etc. Some data can be identified to be noticeably higher than its surrounding data. These data are called “erroneous” or “outlier” data which is a result of many circumstances discussed in Chapter 2.

The easiest solution to remedy outlier data is by data validation through the penalized least square method. This is the “vector validation” function used in PIVlab under the Velocity-based Validation tab [74] shown in Figure 35.

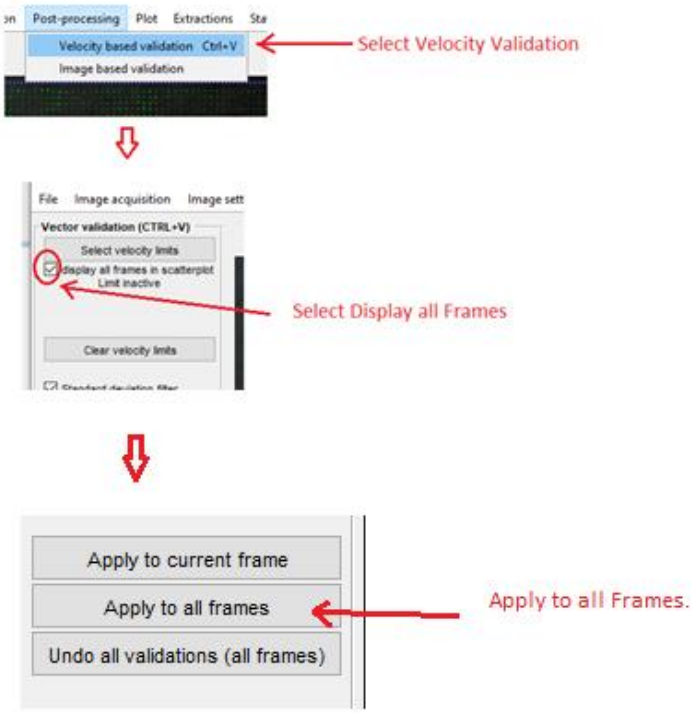

Figure 35: Vector validation in PIVlab

The selection of valid vectors is done manually by drawing a “square” marking the valid vectors and applying this to all the frames as exhibited in Figure 35. Figure 36 shows the selected valid vectors within the orange box.

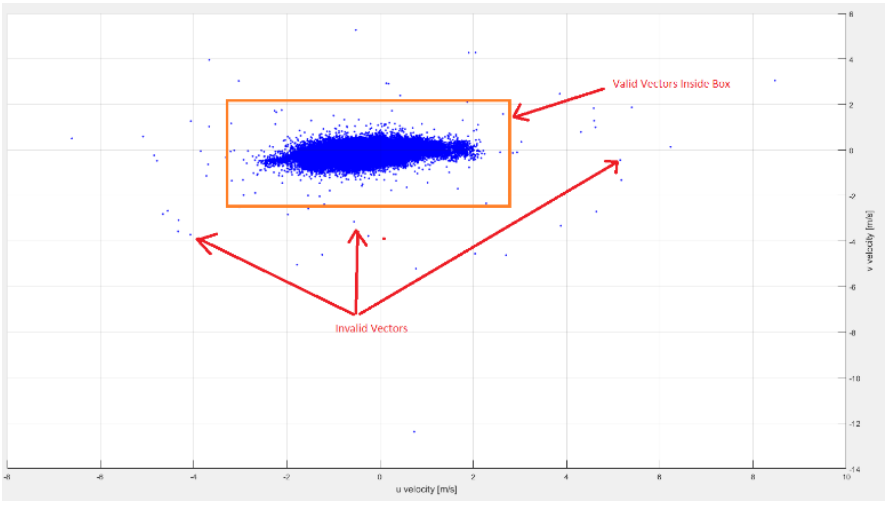

Figure 36: Valid vector selection

Figure 37 shows the result of applying vector validation. The second picture below shows the vector-corrected picture with large or erroneous data that has been removed and replaced with interpolated data.

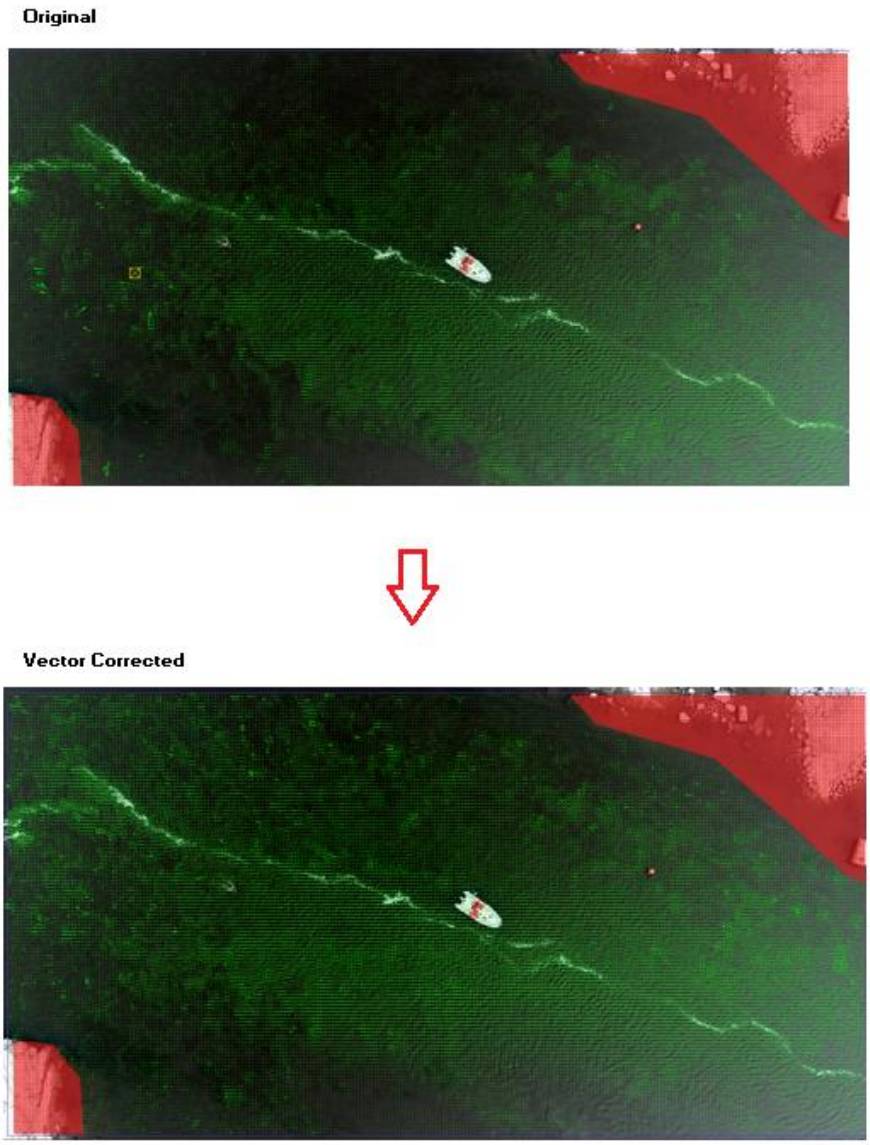

Figure 37: Summary of vector validation

3.5.2 OpenPIV

OpenPIV is an open-source DPIV software that can be used without licensing. It was first created in 1999 and used several programming languages with multiple releases before settling to just one programming language in 2020 using Python [75]. The OpenPIV version used in this thesis is the initial version which did not have a GUI. Thus, most settings are manually coded and will require some Python programming understanding. Figure 38 shows the OpenPIV main screen without GUI.

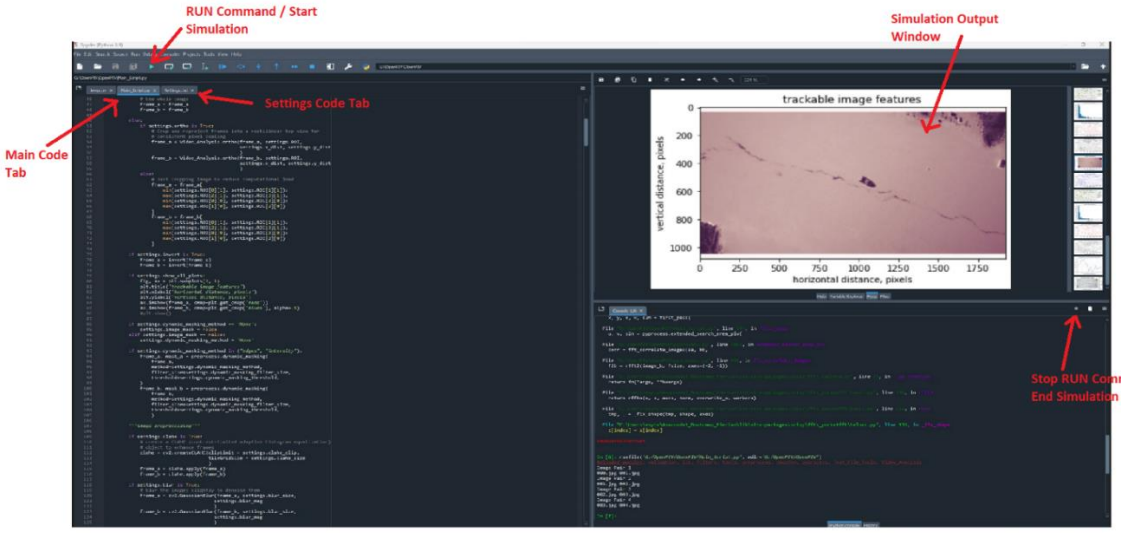

Figure 38: OpenPIV main screen

OpenPIV can be assessed by installing Anaconda, going into the Anaconda Navigation Screen, and launching the Spyder application. Figure 39 displays the Anaconda Navigator Menu were the Spyder app can be found.

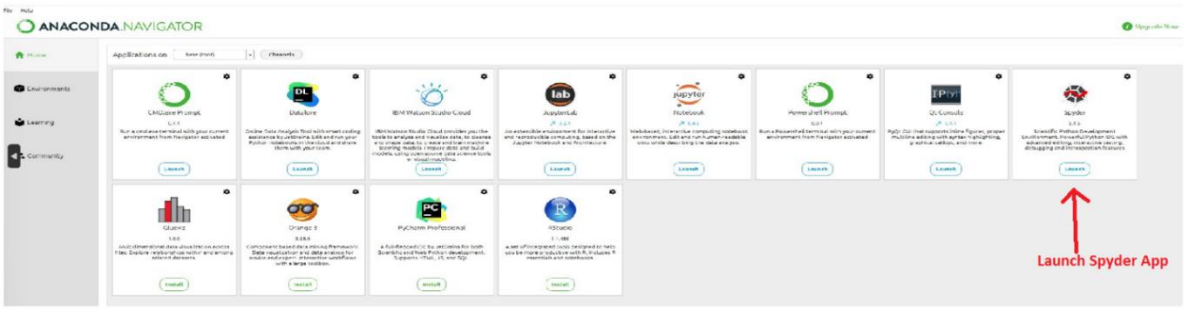

Figure 39: Anaconda navigator menu

Chapter 4: Results and discussion

4.1 CHTTC area of interest (AOI) velocity vector and streamline results

Figure 40 shows the three sites labelled as buoy 1, 2 and 3 at the CHTTC. The whole of Figure 40 is the AOI. Also note that velocities at the CHTTC are typically up to 2.5 m/s but can be as low as 0.5 m/s or lower in drought years like summer 2022 and 2023.

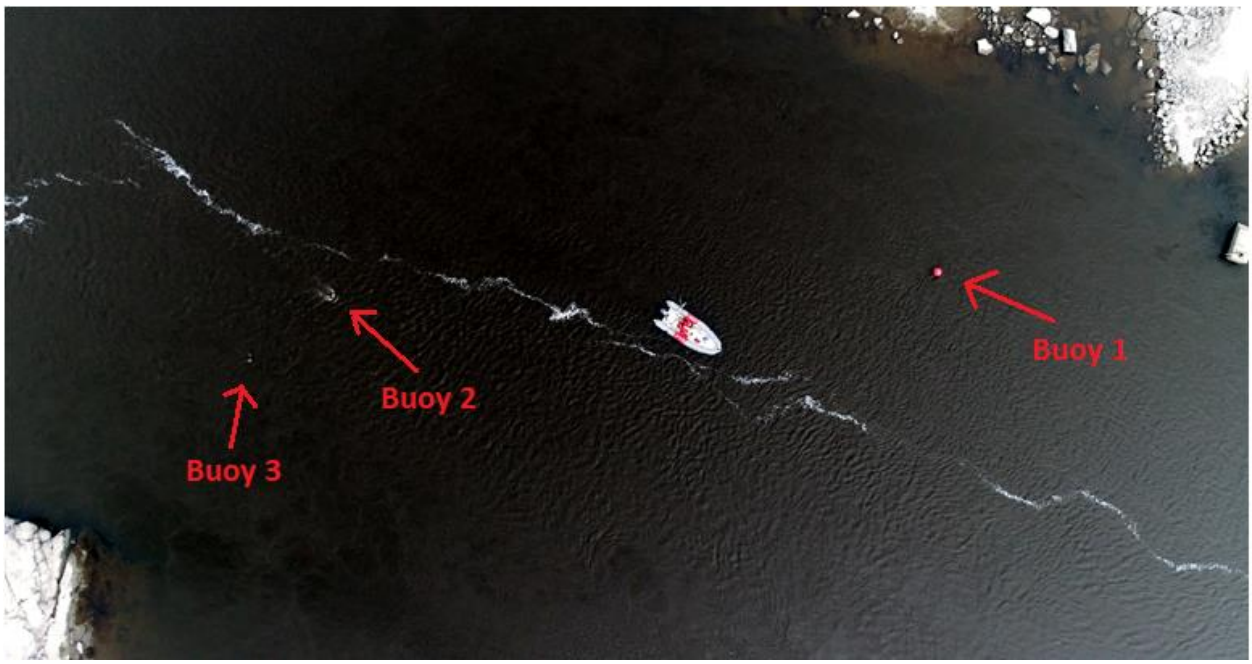

Figure 40: Site buoy locations

The green arrows in Figure 41 depict the resulting velocity vectors on the water surface after PIVlab simulation with vector correction applied. It also shows the masked areas in red that are omitted from the PIVlab analysis. All velocity vectors in green are caused by natural water surface ripples and no particle seeding were carried out during the experiment.

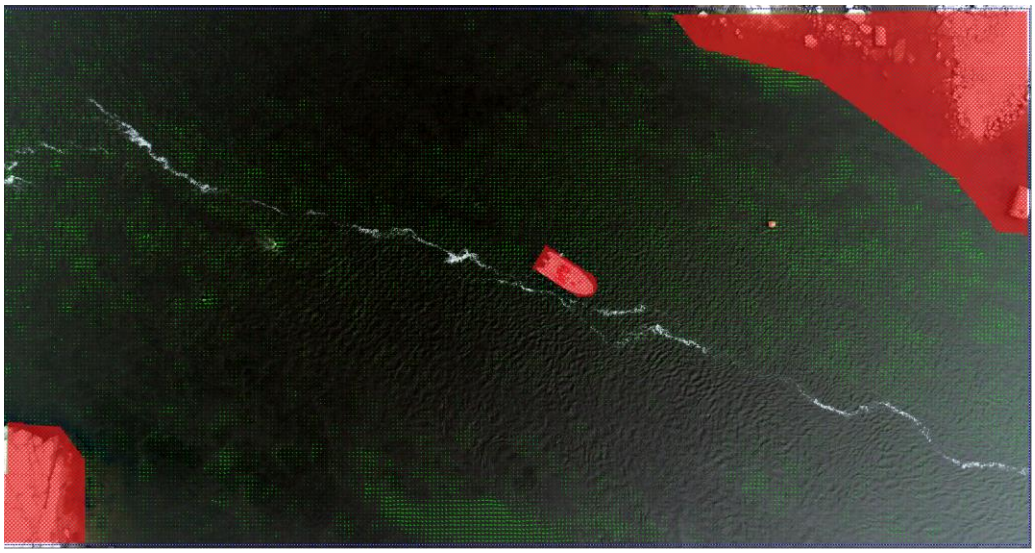

Figure 41: Masked in red and velocity vectors in green

The color bar located on the west side of Figure 42 shows the color interpretation of the different velocity magnitudes after data validation. The yellow lines depict the streamline path of water.

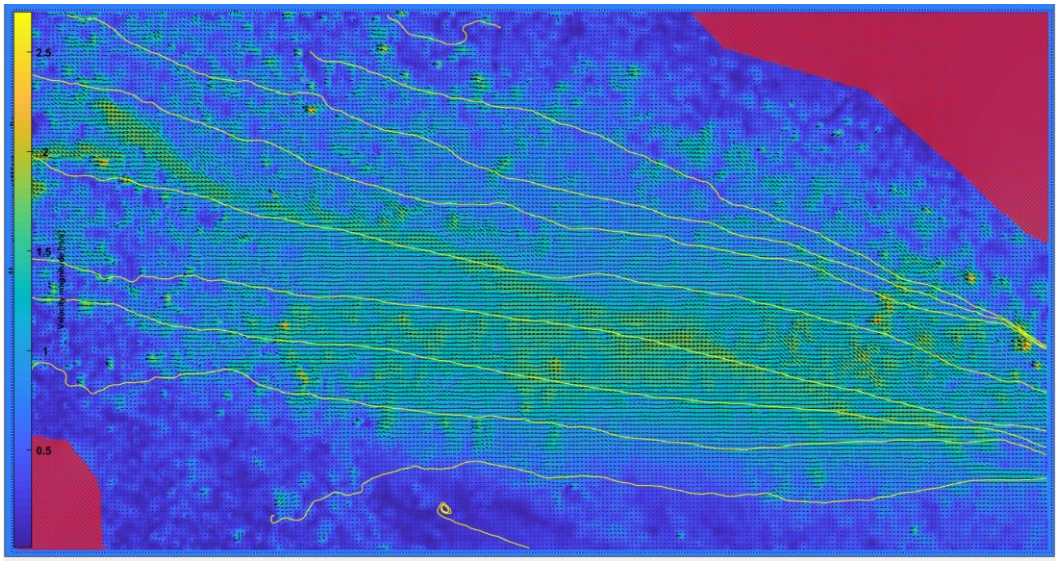

Figure 42: Velocity magnitude color bar and the streamlines.

4.1.1 Site buoy 1 PIVlab results

Table 8: Buoy 1 results (m/s) span of one minute

Buoy 1					
	ADV	PIVlabs (no vector removal)	% Difference Non-Calibrated Vectors with ADV	PIVLabs (Vector Calibrated)	% Difference Calibrated Vectors with ADV
1	0.096	0.225	134.833	0.225	134.833
2	0.110	0.159	44.223	0.113	2.670
3	0.101	0.132	31.093	0.132	31.093
4	0.080	0.107	34.275	0.107	34.275
5	0.085	0.093	9.541	0.089	5.124
6	0.067	0.056	16.652	0.065	2.679
7	0.099	0.098	1.264	0.098	1.264
8	0.078	0.131	69.124	0.059	24.497
9	0.039	0.038	0.987	0.067	73.532
10	0.100	0.109	9.218	0.109	9.218
11	0.104	0.117	13.324	0.101	2.473
12	0.144	0.136	5.702	0.148	2.615
13	0.139	0.138	1.033	0.138	1.033
14	0.102	0.091	11.135	0.095	6.879
15	0.101	0.151	49.990	0.109	8.492
16	0.122	0.110	10.057	0.118	3.505
17	0.118	0.358	203.605	0.142	20.475
18	0.154	0.171	11.404	0.161	4.347
19	0.177	0.187	5.460	0.162	8.832
20	0.176	0.183	4.191	0.171	2.856
Average =	0.110	0.140	27.388	0.120	9.928

Table 8 presents the data from Buoy 1. The ADV river velocity ranges from 0.039 m/s to a maximum of 0.177 m/s. The PIVlab simulations show non-optimized river velocity data ranges from 0.038 to 0.358 m/s. This translates to a difference of 0.99 to 203.61% discrepancy from the ADV reading, with an average of 27.4%. After optimizing the data, the data now has a river

surface velocity range from 0.059 to 0.225 m/s. The optimized data velocities now have a difference from 1.26 to 134.83% with an average of 9.93% from the ADV-measured river velocity. The optimized vectors have an average velocity of 0.12 m/s versus 0.14 m/s for non-optimized velocity and are 0.01 m/s and 0.03 m/s respectively away from the average ADV reading of 0.11 m/s.

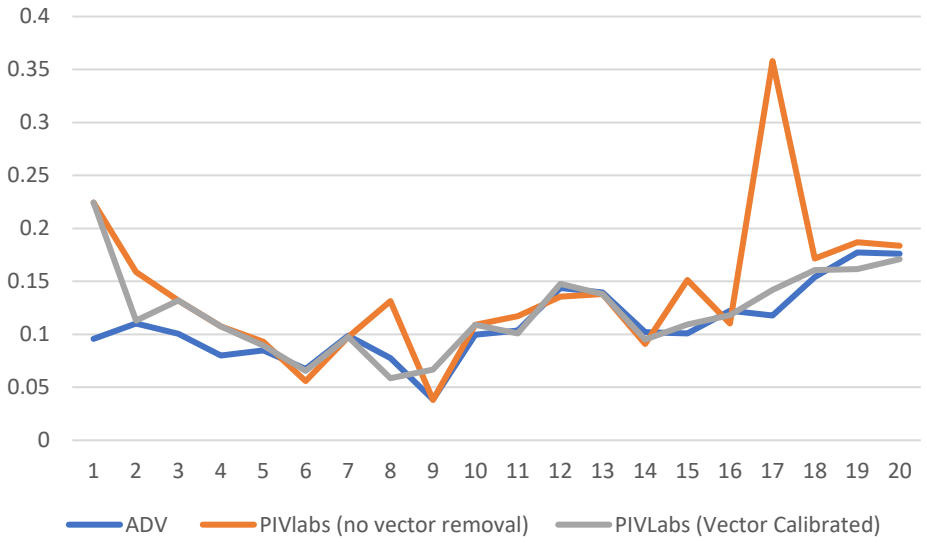

Figure 43: Velocity comparison chart (Buoy 1)

Figure 43 shows how the vector optimized data results are closer to the reference ADV data. In addition, the vector optimized data vectors show less shifting by removing erroneous data that is too far from the mean vector. Figure 44 shows how the removal of erroneous data and replacement of interpolated data has resulted with the optimized data being near identical to the ADV results.

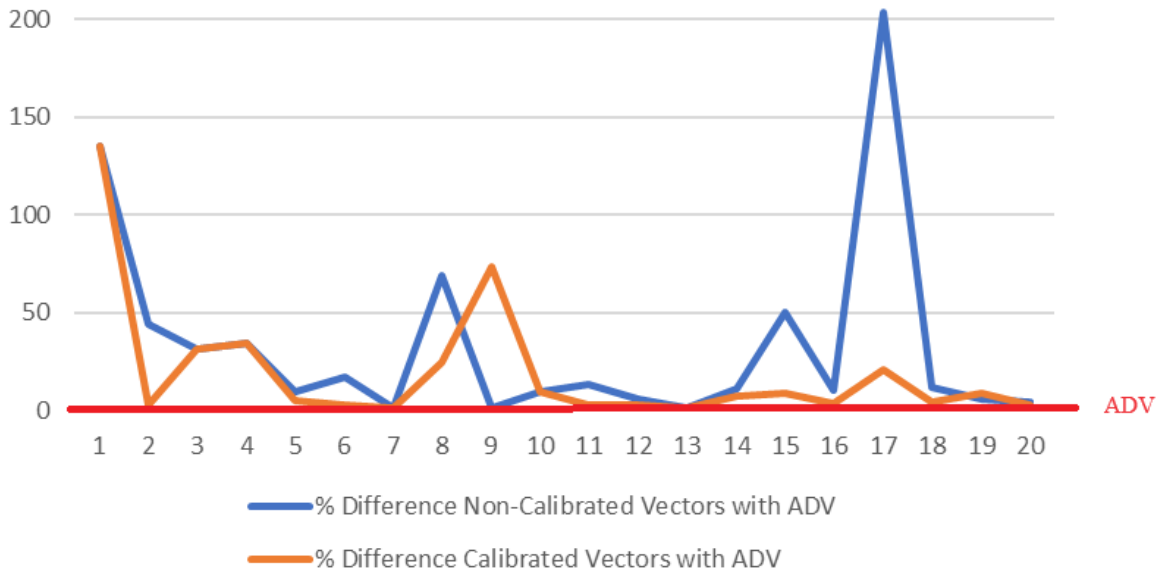

Figure 44: % Difference to ADV (Buoy 1)

4.1.2 Site buoy 2 PIVlab results

Table 9: Buoy 2 results (m/s) span of one minute

Buoy 2					
	ADV	PIVlabs (no vector removal)	% Difference Non-Calibrated Vectors with ADV	PIVLabs (Vector Calibrated)	% Difference Calibrated Vectors with ADV
1	0.144	0.169	17.603	0.169	17.603
2	0.144	0.160	11.341	0.162	12.696
3	0.167	0.152	8.499	0.169	1.471
4	0.166	0.154	7.198	0.166	0.169
5	0.179	0.180	0.779	0.175	2.078
6	0.148	0.135	8.993	0.135	8.993
7	0.145	0.143	1.397	0.143	1.397
8	0.149	0.134	9.570	0.132	11.224
9	0.134	0.148	10.544	0.138	2.450
10	0.128	0.158	23.131	0.129	0.685
11	0.144	0.159	11.094	0.145	1.317
12	0.146	0.144	1.132	0.144	1.132
13	0.151	0.147	2.805	0.147	2.805
14	0.146	0.134	8.018	0.144	0.926
15	0.138	0.136	1.361	0.136	1.361
16	0.141	0.143	1.558	0.143	1.558
17	0.118	0.141	19.821	0.128	9.311
18	0.158	0.147	7.058	0.156	1.065
19	0.171	0.164	4.087	0.167	2.149
20	0.184	0.179	2.767	0.176	3.905
Average =	0.150	0.151	0.999	0.150	0.270

Table 9 displays the velocity data from Buoy 2. The ADV measurements range from 0.118 m/s to 0.184 m/s with an average of 0.150 m/s, while the simulated non-calibrated water surface analysis from PIVlab ranges from 0.134 m/s to 0.180 m/s with an average of 0.151 m/s. The

optimized vectors now have a minimum of 0.128 m/s to a maximum of 0.176 m/s with an average of 0.150 m/s. The average optimized velocity now shows a negligible difference to the average ADV reading at 0.27% difference from the ADV average velocity data.

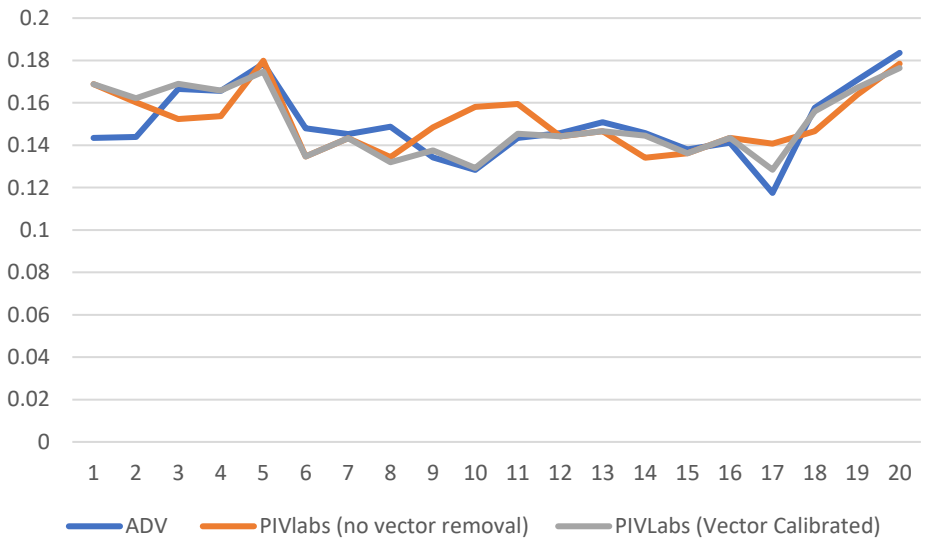

Figure 45: Velocity comparison chart (Buoy 2)

Figure 45 demonstrates how the optimized and non-optimized vectors compare to the reference ADV vector data. The optimized data is much closer to the ADV velocity data results. While the raw data without vector optimization has data that fluctuates more, and vectors further from the reference ADV results. Figure 46 shows how the optimized vector numbers are closer to the ADV results than the non-optimized vectors.

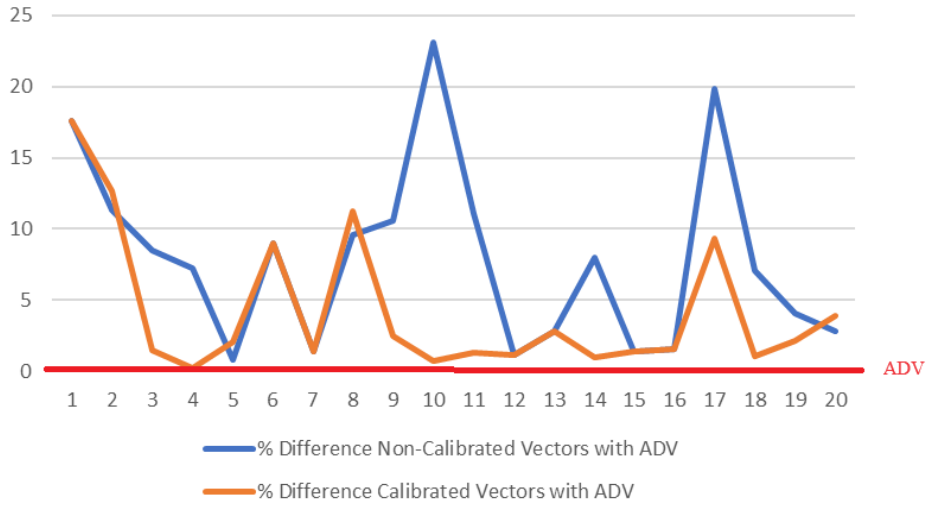

Figure 46: % Difference from ADV results (Buoy 2)

4.1.3 Site buoy 3 PIVlab results

Table 10: Buoy 3 results (m/s) span of one minute

Buoy 3					
	ADV	PIVlabs (no vector removal)	% Difference Non-Calibrated Vectors with ADV	PIVLabs (Vector Calibrated)	% Difference Calibrated Vectors with ADV
1	0.068	0.127	88.207	0.127	88.207
2	0.065	0.099	51.407	0.106	62.064
3	0.080	0.076	5.012	0.092	15.012
4	0.089	0.086	2.847	0.082	7.311
5	0.136	0.120	11.820	0.138	1.835
6	0.156	0.159	1.725	0.159	1.725
7	0.173	0.158	8.643	0.187	7.685
8	0.158	0.141	10.717	0.157	0.114
9	0.195	0.170	12.809	0.170	12.809
10	0.223	0.244	9.623	0.226	1.539
11	0.210	0.190	9.457	0.181	13.580
12	0.195	0.200	2.594	0.200	2.594
13	0.182	0.168	7.592	0.180	1.193
14	0.178	0.154	13.457	0.181	1.959
15	0.164	0.160	2.303	0.164	0.165
16	0.145	0.163	12.464	0.141	2.270
17	0.133	0.155	16.729	0.155	16.729
18	0.128	0.111	13.690	0.127	0.663
19	0.115	0.112	2.594	0.117	2.237
20	0.128	0.128	0.210	0.126	2.097
Average =	0.146	0.146	0.035	0.151	3.378

Buoy 3 velocity data are shown in Table 10. ADV velocity data ranges from 0.065 m/s to 0.223 m/s. PIVlab non-optimized velocities are from 0.076 m/s to 0.244 m/s with an average of 0.146 m/s, while optimized vectors show a lower peak velocity and vector velocities ranging from .082 m/s to 0.226 m/s with an average of 0.151 m/s. The average ADV measured velocity

is 0.146 m/s which is 0.005 m/s away from the average of the optimized PIVlab data result. Figure 47 shows how close the PIVlab and ADV velocity results are to each other.

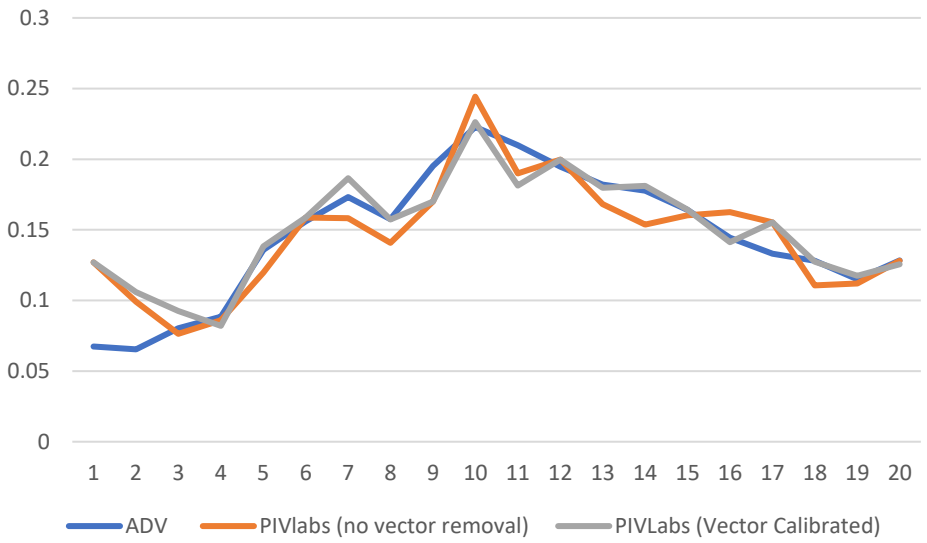

Figure 47: Velocity comparison chart (Buoy 3)

Finally, Figure 48 indicates optimized results in orange showing a slight fluctuation before settling near 0%, which is the ADV reference result. This indicates the effectivity of the interpolated data used by the PIVlab algorithm.

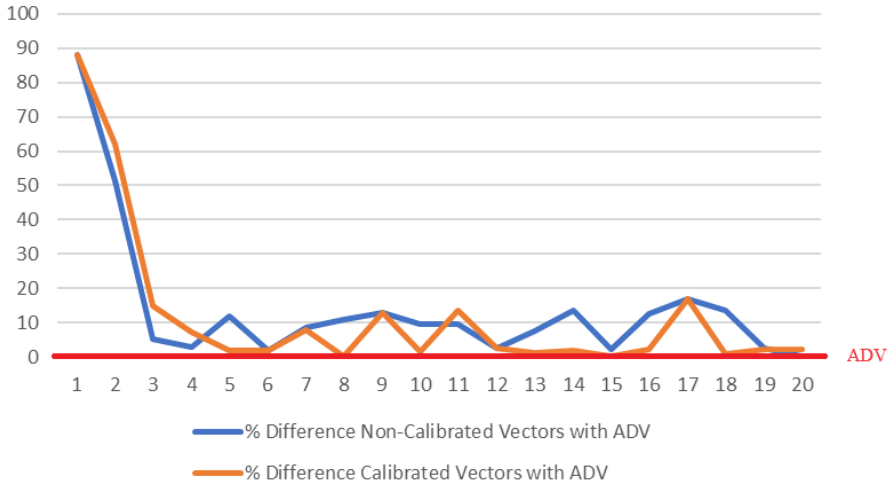

Figure 48: % Difference from ADV results (Buoy 3)

4.1.4 Site OpenPIV results

The velocity data from OpenPIV can be approximated from the output chart it generates after simulation. In addition, there was no option to pick an area in the final simulation results to find velocity results for specific areas. Hence, velocity can only be approximated based on the generated OpenPIV charts shown in Figure 49. In Figure 49, the yellow vector line is the maximum surface velocity at 1.5 m/s, and the purple vector line is the minimum surface velocity at 0.05 m/s.

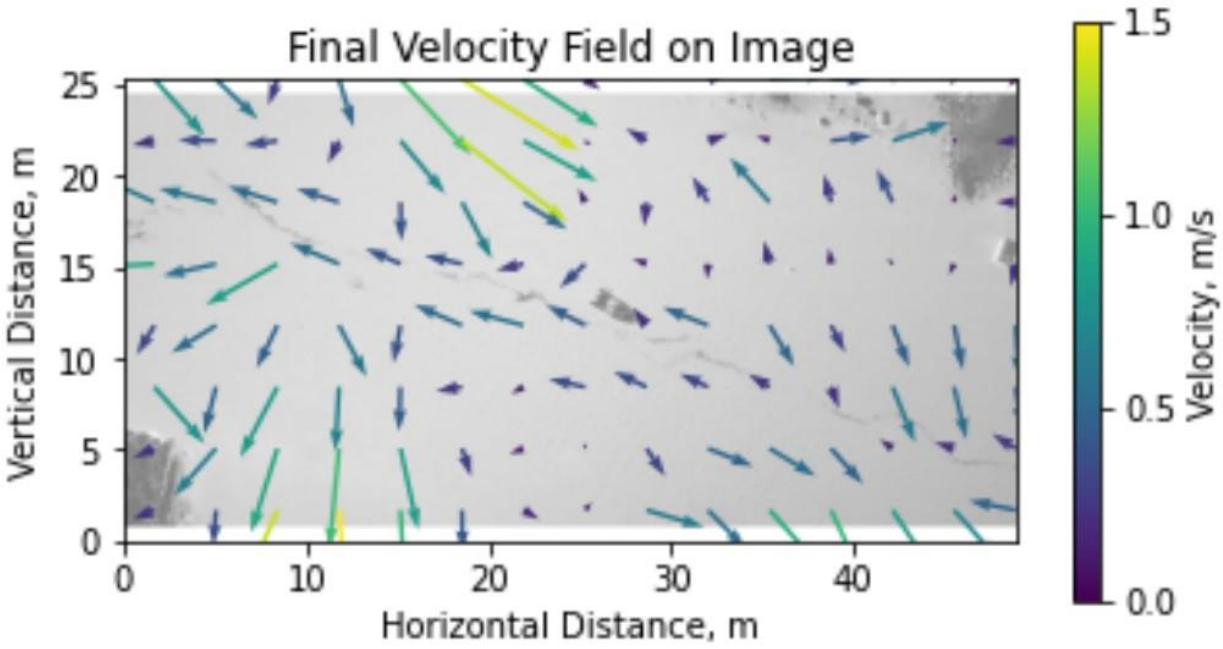

Figure 49: OpenPIV final velocity results

The final mid-channel water surface velocity is shown in Figure 50. The chart shows a minimum velocity of 0.02 m/s to a maximum of 0.55 m/s.

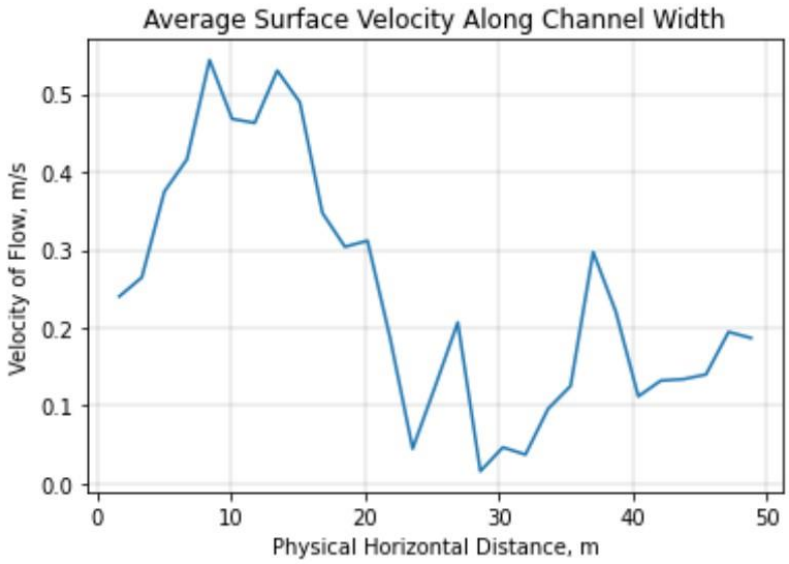

Figure 50: OpenPIV mid-channel final velocity result

4.1.5 Site PIVlab to OpenPIV result comparison on CHTTC buoys.

To compare the results of OpenPIV and PIVlab, a polyline was drawn along the width of the image in PIVlab analysis to duplicate the mid-channel velocity output analysis of OpenPIV. Figure 51 shows the location of the Polyline in PIVlab.

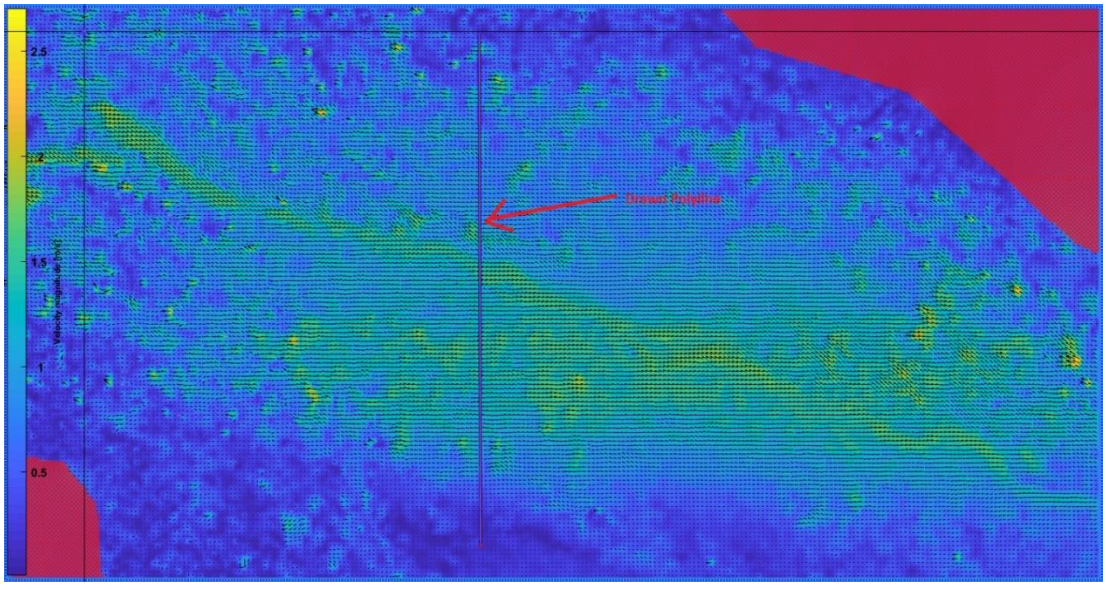

Figure 51: Polyline location in PIVlab simulation

The superimposed velocity results for both PIVlab and OpenPIV along the mid-channel is shown in Figure 52.

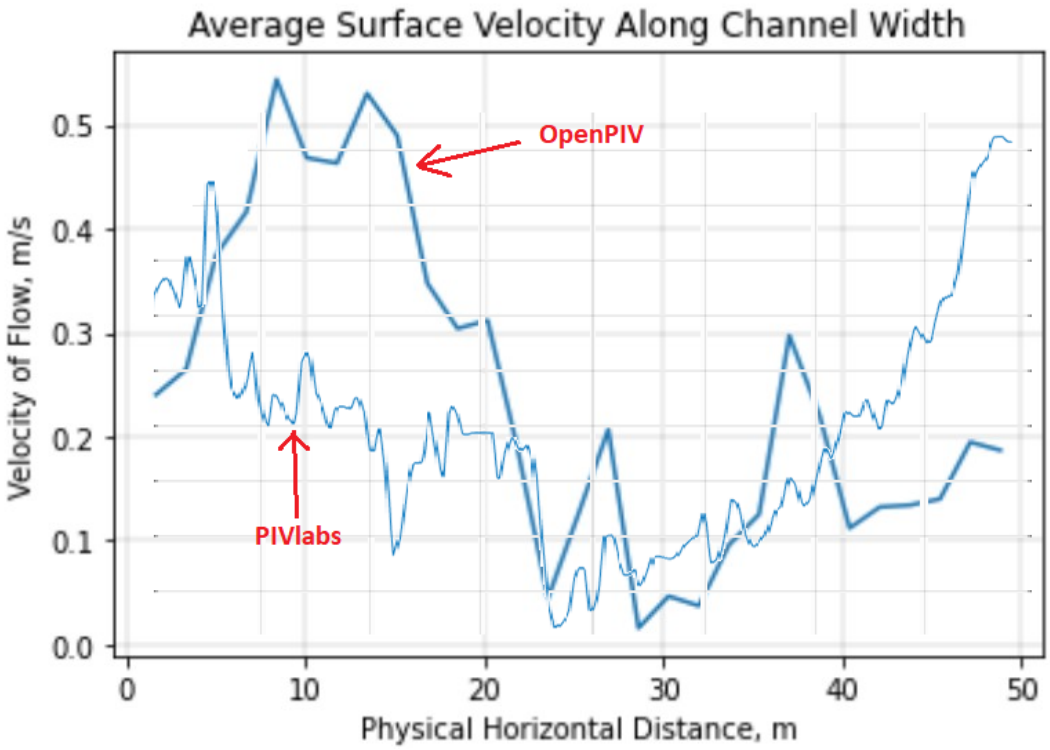

Figure 52: DPIV velocity result comparison

The PIVlab river surface velocity results are lower than OpenPIV. However, both PIVlab and OpenPIV share a similar velocity profile with the initial velocity increasing, then lowering, and then finally increasing. Both simulations have a minimum velocity of 0.025 m/s, while the maximum velocity for PIVlab is 0.45 m/s and OpenPIV being slightly higher at 0.55 m/s. One reason for the discrepancy between the simulation results is that there are no settings in OpenPIV to change the IA size multiple times. Even the latest OpenPIV version does not support multiple IA's as of this writing. This limits the discreet Fourier transform passes to one versus four for PIVlab. The four passes in PIVlab are set to 256, 128, 64 and 32, while OpenPIV is set to 128 with only one pass. Another reason is the location of the polyline, which cannot be set exactly where OpenPIV places its polyline during the simulation process.

Finally, by being able to set IA's bigger and then making it gradually smaller to increase the number of passes increases the accuracy of the simulation results [74] in PIVlab where this option is unavailable in OpenPIV. Thus, PIVlab results are more accurate than OpenPIV since PIVlab simulated with several passes with varying interrogation areas. In addition, PIVlab can mask unused areas in the image that can affect the data negatively, whereas OpenPIV has no such capability.

4.2 Laboratory water tunnel results

4.2.1 General PIVlab settings

The clear water surface texture of the water turbine experiment shows additional image pre-processing is necessary. Figure 53 shows light reflections from overhead lights have oversaturated several areas in the image frame. In addition, the clear water surface made the water surface texture less visible since no particle seeding was implemented during the experiment. Thus, extra image pre-processing was needed.

Finally, the water tunnel velocity is set at 0.4 m/s and is ADV calibrated.

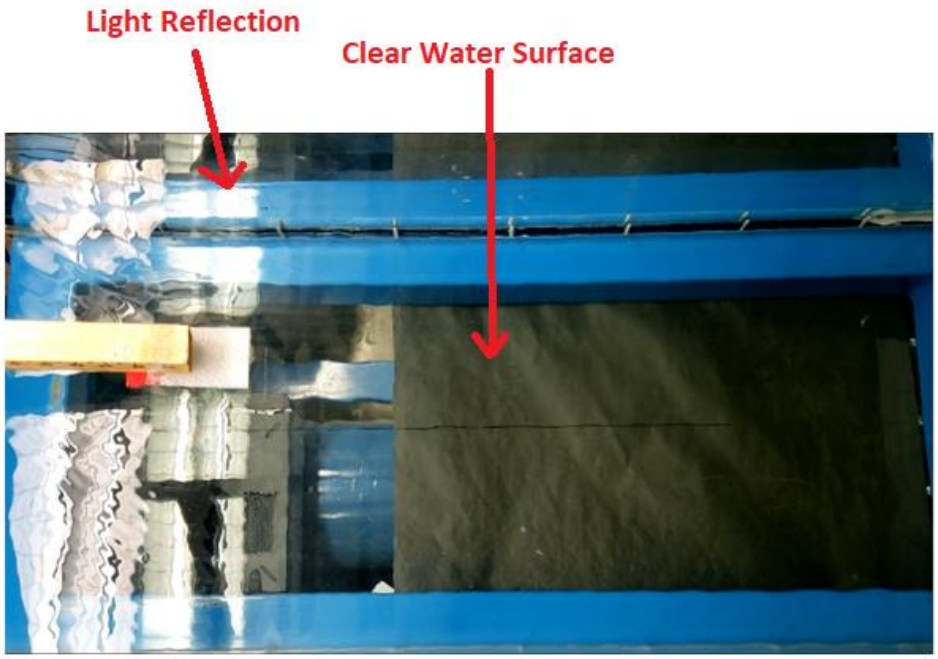

Figure 53: Untouched water surface image in water turbine

The first pre-processing applied was CLAHE. Figure 54 shows the effects. Water surface texture and contrast are now visible.

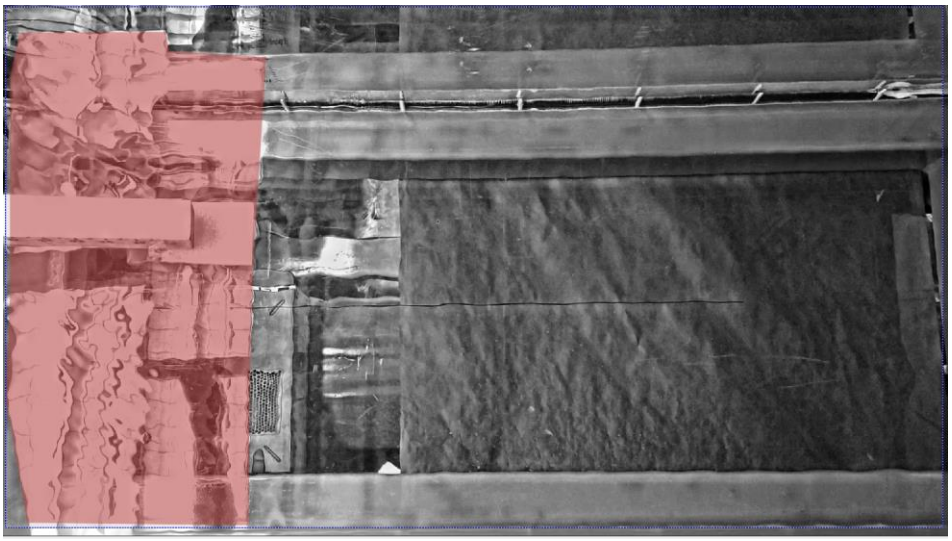

Figure 54: CLAHE effect to water tunnel surface image

The second pre-processing applied was the high-pass filter. Figure 55 below shows the effect of high-pass filter in the image. Since the high-pass filter seemed too aggressive and removed significant details in the image after it was applied, it was deactivated and reverted to CLAHE without the high-pass filter.

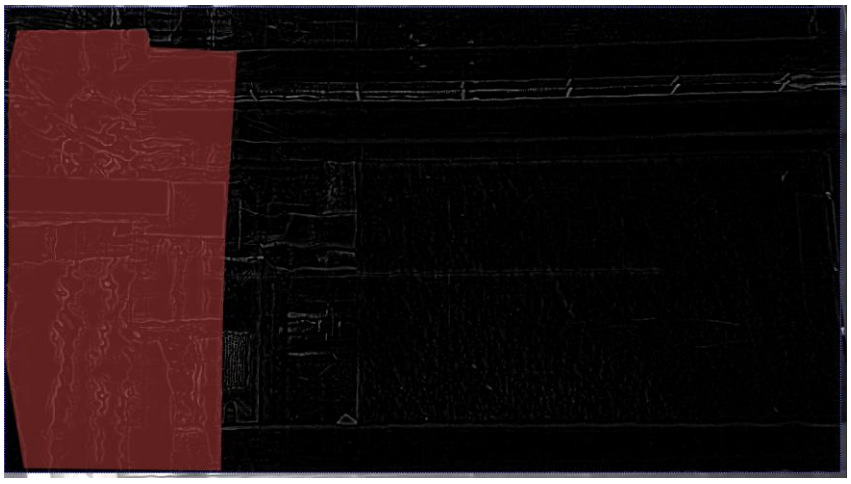

Figure 55: Water tunnel surface after high-pass application

The final image pre-processing applied was enabling intensity capping. This allows us to limit several areas in the image that are too bright, such as the light reflections. The final image is shown in Figure 56 after intensity capping was applied.

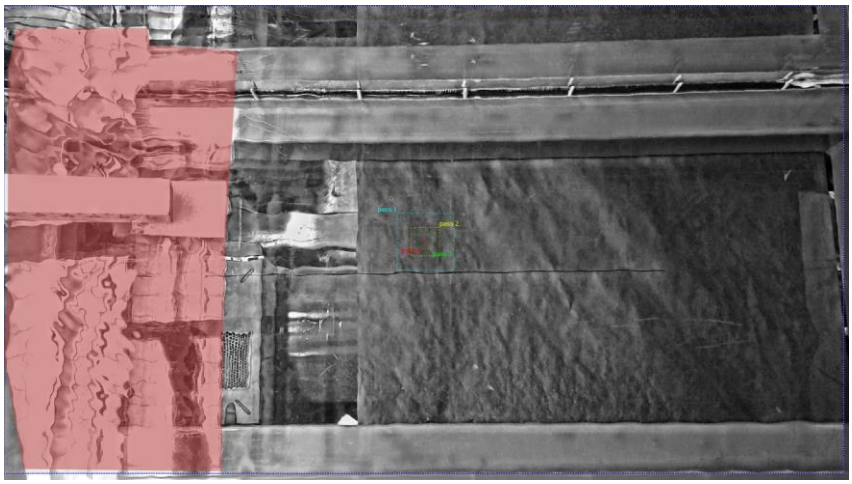

Figure 56: Final water tunnel surface image after image pre-processing

Figure 56 shows the settings of adding the FFT algorithm to speed up the LSPIV processing. Four passes were enabled to improve the simulation results with each pass smaller than the previous pass as shown in Figure 56. The four pass settings for the water tunnel were 128, 64, 32, and 16. Figure 57 shows the settings window.

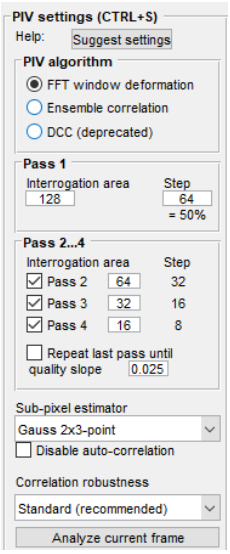

Figure 57: Water tunnel PIV settings

4.2.2 PIVlab water tunnel set velocity 0.4 m/s results and discussion

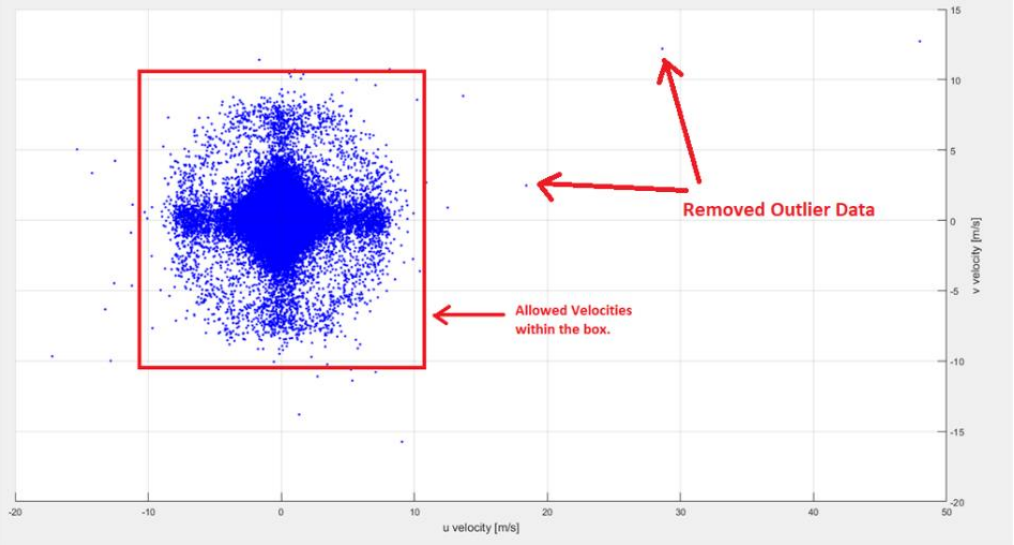

Figure 58: Allowed and outlier data

Figure 58 shows a red box which is the allowed data or valid data. Anything within the box is considered good data, while anything outside-the-box data are considered erroneous or outlier data. This outlier data is deleted and replaced with interpolated data. Figure 59 shows the original versus validated image incorporating the interpolated data.

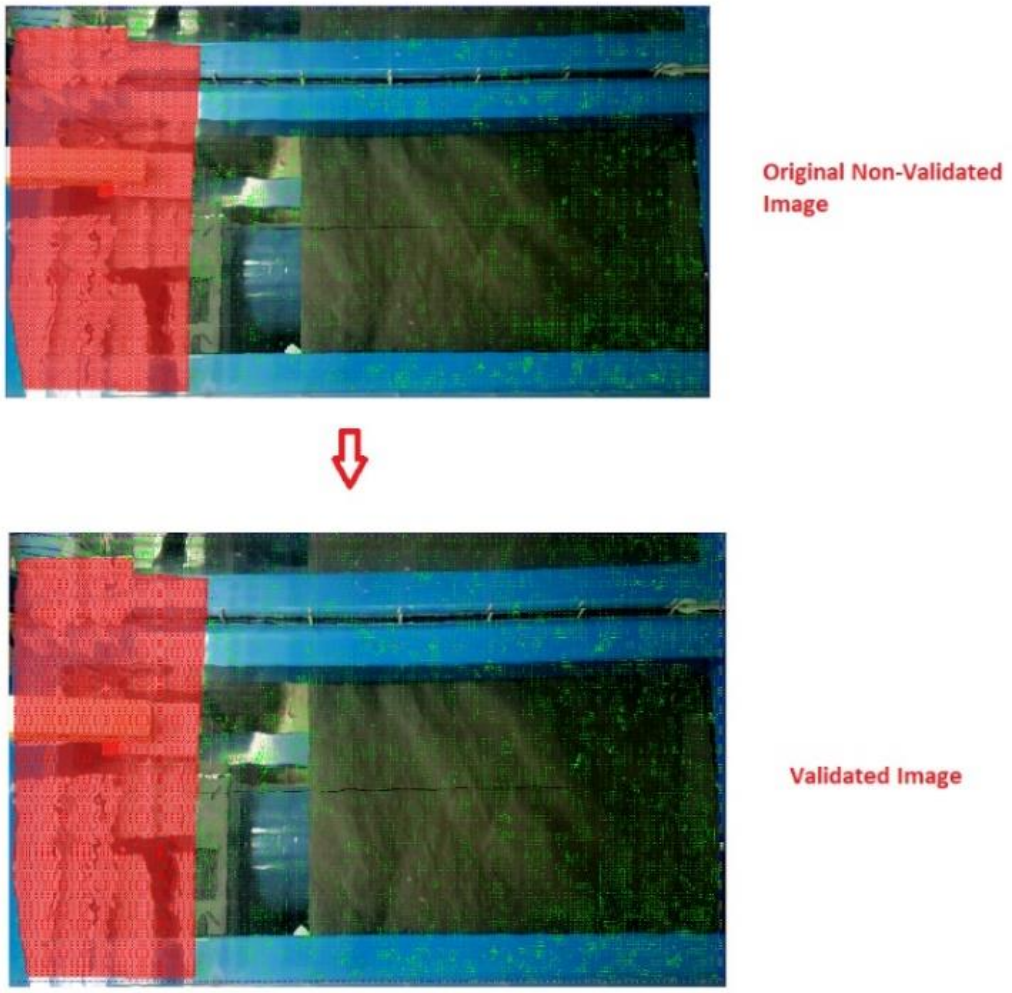

Figure 59: Water tunnel 0.4 m/s validated vs non-validated image

Figure 60 shows the water surface velocity of the water tunnel. The color bar located in the left side of the image shows the meaning of the different colors in the image representing the water surface velocity. The water tunnel velocity was set to 0.4 m/s, is which is reflected in the PIVlab result in Figure 60, which shows predominantly blue which is approximately 0.4 m/s.

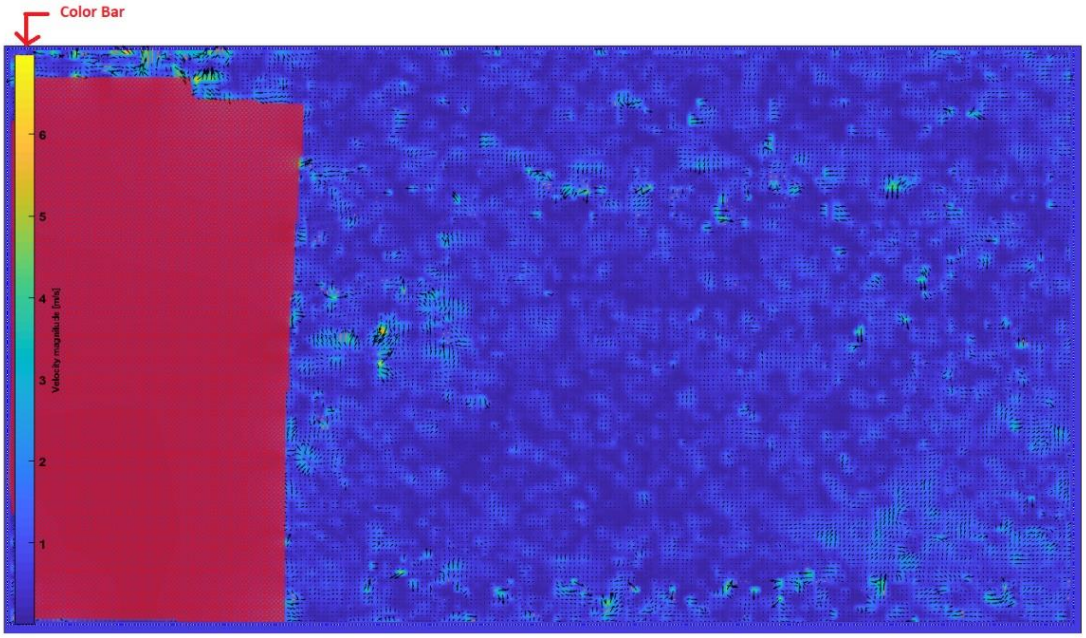

Figure 60: Water tunnel 0.4 m/s velocity magnitude

Table 11 below shows the LSPIV simulation results for the water tunnel set at an ADV calibrated 0.4 m/s. Without data optimization, PIVlab's simulated velocity result show an average water surface velocity of 0.431 m/s, and is 7.82% away from the reference 0.4 m/s. The optimized average velocity is 0.419 m/s meaning a difference of 4.71% from the set water tunnel velocity of 0.4 m/s. Vector optimized data shows clear improvement over the non-optimized vector data.

Table 11: Water tunnel LSPIV results span of one minute

Water Tunnel Speed 0.4m/s					
	ADV	PIVlabs (no vector removal)	% Difference Non-Calibrated Vectors with ADV	PIVLabs (Vector Calibrated)	% Difference Calibrated Vectors with ADV
1	0.400	0.358	10.460	0.412	3.042
2	0.400	0.353	11.708	0.361	9.775
3	0.400	0.432	8.010	0.432	8.010
4	0.400	0.615	53.718	0.419	4.735
5	0.400	0.436	9.090	0.397	0.805
6	0.400	0.357	10.735	0.394	1.598
7	0.400	0.297	25.680	0.330	17.480
8	0.400	0.551	37.718	0.444	10.938
9	0.400	0.385	3.663	0.412	2.985
10	0.400	0.343	14.265	0.403	0.645
11	0.400	0.367	8.203	0.428	7.003
12	0.400	0.493	23.345	0.450	12.595
13	0.400	0.686	71.465	0.622	55.445
14	0.400	0.404	0.935	0.404	0.935
15	0.400	0.463	15.640	0.396	1.075
16	0.400	0.493	23.138	0.359	10.353
17	0.400	0.324	18.953	0.415	3.712
18	0.400	0.361	9.765	0.419	4.870
19	0.400	0.559	39.743	0.451	12.765
20	0.400	0.348	12.933	0.431	7.700
Average =	0.400	0.431	7.822	0.419	4.715

Figure 61 shows the line graph of Table 11, and illustrates the optimized data in grey is much closer to the set water tunnel speed of 0.4 m/s in blue than the non-optimized data in orange. This indicates that using the optimized data is more accurate than the raw data where outlier data are still present.

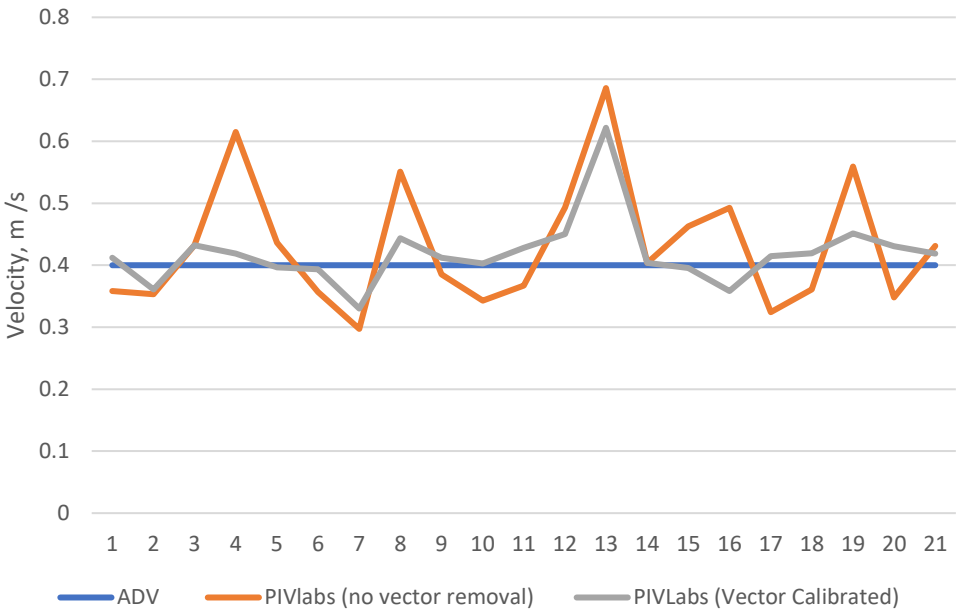

Figure 61: Water tunnel 0.4 m/s velocity comparison chart

4.2.3 OpenPIV water tunnel set velocity 0.4 m/s results and discussion

As mentioned in Section 4.1.4, OpenPIV velocity can be approximated based on the image charts that it provides after the OpenPIV simulation. Figure 62 shows OpenPIV simulation result where the final maximum velocity is 2.5 m/s shown in yellow vector, and the minimum velocity is approximately 0.25 m/s shown in purple vector.

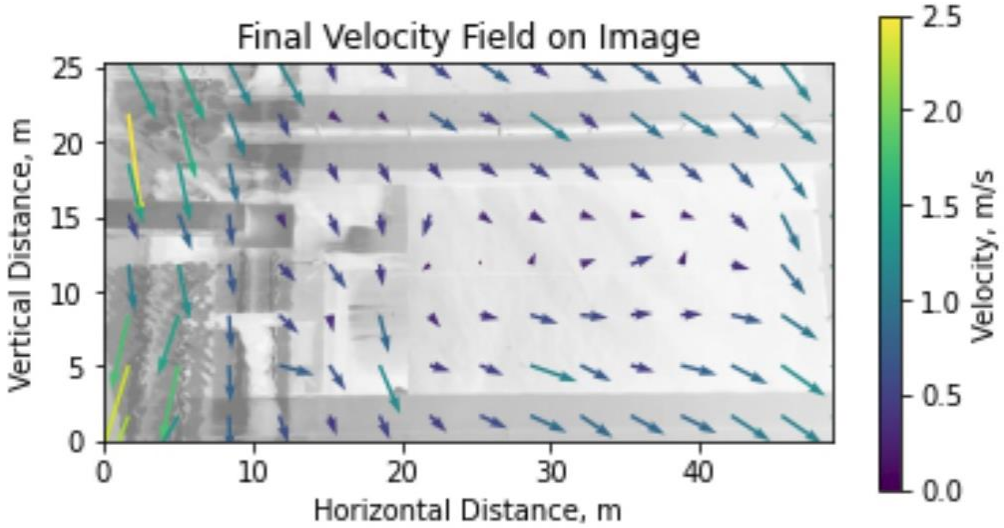

Figure 62: OpenPIV final velocity for 0.4 m/s

The OpenPIV simulation shows a higher maximum water surface velocity when compared to PIVlab results. This can be the result of the reflected light affecting the OpenPIV analysis since there was no option to mask these areas. In addition, the central part of Figure 62 were there are no reflected lights affecting the simulation process shows more purple or around 0.4 m/s which is what we expect since the water turbine was set to 0.4 m/s.

4.2.4 PIVlab to OpenPIV water tunnel result comparison

As mentioned in Section 4.1.5, a polyline must be drawn in PIVlab to find surface velocity along the mid-channel. Figure 63 shows the location of the polyline.

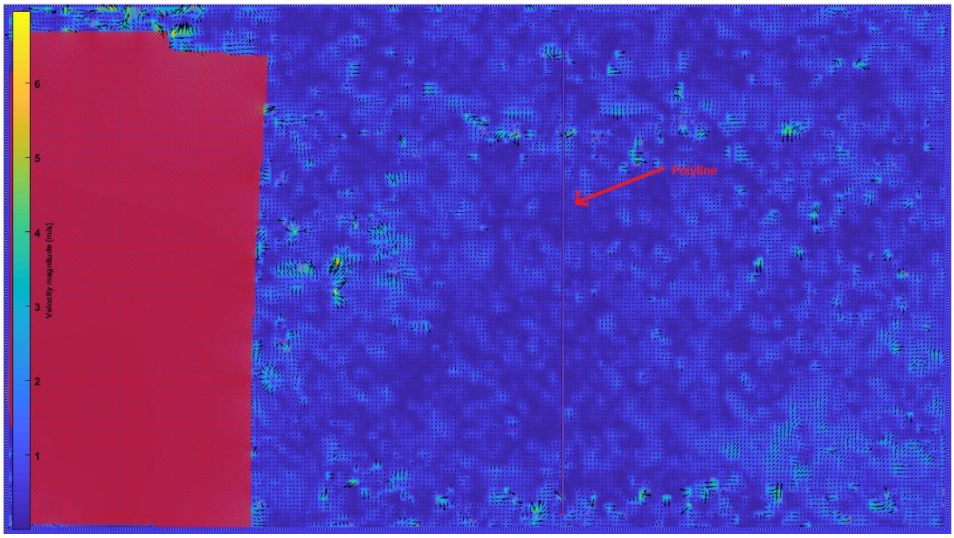

Figure 63: PIVlab polyline location for water tunnel simulation

Figure 64 shows the superimposed velocity results from both PIVlab and OpenPIV. Both LSPIV simulations show an almost identical minimum water surface velocity of 0.3 m/s and a maximum of 1.5 m/s. However, the velocity profile for both is not similar with the PIVlab velocity profile fluctuating more. As mentioned in Section 3.4.1, PIVlab has several options such as masking, varying IA's and multiple passes allowing it to respond faster to different water velocities along the water surface. These options were unavailable with OpenPIV.

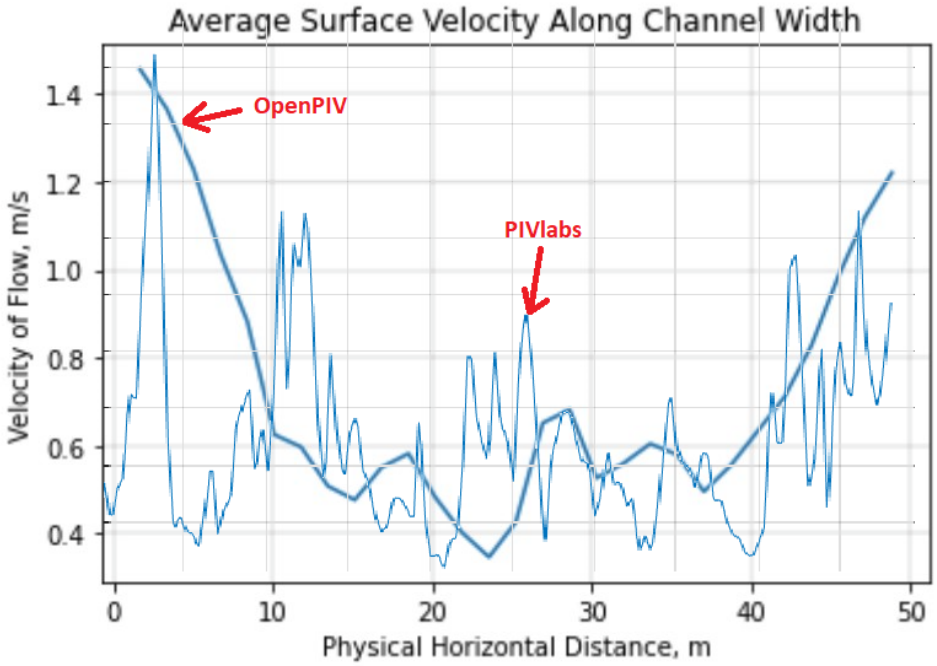

Figure 64: PIVlab to OpenPIV superimposed comparison chart

4.3 Summary data results

Results from CHTTC site and water tunnel experiments show PIVlab and OpenPIV results to have an average of 5% difference from the measured reference ADV velocity data after the resulting LSPIV velocity data were optimized. Such error was obtained by averaging velocities over 1 min or 1,800 images. Site Buoy 1 recorded the lowest LSPIV analysis accuracy with an average vector optimized velocity difference of 10% from the reference ADV data results, while site Buoy 2 recorded the highest LSPIV accuracy at 0.3%, and site Buoy 3 at 3.3%. All LSPIV simulations show data improvements after data optimization.

Chapter 5: Conclusion and future work

5.1 Conclusion

This study was conducted to understand if current non-invasive DPIV methods of water surface velocity measurement such as LSPIV can be used as a substitute for current meters in water surface velocity measurement.

Based on the research results collected during the study, we can conclude the following:

- Capturing proper images / videos is crucial to the accuracy of the DPIV analysis. Factors such as:
    - Poor weather such as high winds can affect water surface ripples which can introduce outlier vectors and create much higher vectors than the surrounding vectors. Additionally, foggy weather and Sun reflection make it difficult to trace surface water ripples and will modify LSPIV analysis results.
    - Good lighting conditions where clear natural water surface ripples are crucial in LSPIV analysis.
- In good weather conditions, installed continuous monitoring cameras in river basins used to provide river information can be used to provide quantitative data such as water surface velocity by utilizing LSPIV if these images are orthorectified.
- Capturing images at Nadir simplifies the vector analysis and creates better results by removing the orthorectification process. By doing away with the orthorectification process, several factors that can exert an influence on the DPIV analysis, such as: lens distortion and image skewing are prevented.
- It was observed that increasing the number of passes when using FFT algorithm enhances data accuracy. PIVlab showed results almost 20% closer to the ADV results and fluctuated less compared to OpenPIV which did not have the multiple pass option.
- PIVlab simulated average optimized velocity results came as close as 0.001m/s to the ADV measured average water surface velocity.
- This research demonstrates that using civilian-grade drones equipped with image stabilizing gimbals allows sufficient stabilization for LSPIV analysis.

- This research illustrates that unseeded water surface velocity software simulations both in clear water tunnel surface and in open channel river sites will yield results that are very close to ADV measured results.
- Finally, the research shows that the simulated results of PIVlab and OpenPIV show velocity measurements that are within 4% of ADV measurements, especially when data is validated. Thus, it can potentially replace conventional invasive velocity measurement practices that are not only cumbersome but can be life threatening in some conditions.

5.2 Future work

Some recommendations for future work:

- This research was conducted in good weather and the water flow was smooth and consistent. Thus, being able to work in a high-water flow environment such as flooding can be considered in the future if this can be done safely.
- Adding GCP's and water elevation monitors at the CHTTC center will add another way to calibrate vectors. This will also allow the use of more recent and paid for software that can be used to compare the open-source LSPIV software used in this research.
- A drone is used to capture images in this thesis. But most studies use images that are captured by stationary closed-circuit digital cameras located on riverbanks and not by drones flying overhead. Thus, these images often exhibit oblique angles that can distort data accuracy resulting from non-Nadir images. Therefore, future studies on auto image orthorectification are needed on non-Nadir images to increase data accuracy and expedite data processing.
- High velocity water tunnel simulations. This research made several attempts to work on high velocity unseeded water tunnel simulations. However, simulation results encountered several issues such as the water tunnel walls being too close such that water was being thrown in several directions making the simulation results erroneous. Thus, further future investigation is recommended in this matter.

References

[1] M. Brander and G. Davis, "Ecometrica," August 2012. [Online]. Available: https://ecometrica.com/assets/GHGs-CO2-CO2e-and-Carbon-What-Do-These-Mean-v2.1.pdf. [Accessed 17 September 2022].

[2] M. Denchak, "Greenhouse Effect 101," NRDC, 16 07 2019. [Online]. Available: https://www.nrdc.org/stories/greenhouse-effect-101#whatis. [Accessed 25 03 2023].

[3] Q. Schiermeier, "Increased flood risk linked to global warming: Likelihood of extreme rainfall may have been doubled by rising greenhouse-gas levels.," *Nature*, vol. 470, no. 7334, p. 316, 2011.

[4] M. Zastempowski , "Analysis and modeling of innovation factors to replace fossil fuels with renewable energy sources - Evidence from European Union enterprises," *Renewable and Sustainable Energy Reviews*, vol. 178, no. 113262, pp. 87-100, 2023.

[5] Enerdata, "World Energy & Climate Statistics - Yearbook 2022," 2022. [Online]. Available: https://yearbook.enerdata.net/. [Accessed 12 03 2023].

[6] M. Kaltschmitt, W. Streicher and A. Wiese, . Renewable Energy: Technology, Economics and Environment, Berlin: Springer-Verlag, 2007.

[7] J. A. Fay and D. S. Golomb, Energy and the Environment, New York: OXFORD UNIVERSITY PRESS, 2002.

[8] S. BERNAD, . A. GEORGESCU, S.-C. GEORGESCU, R. SUSAN-RESIGA and I. ANTON, "FLOW INVESTIGATIONS IN ACHARD TURBINE," 2008. [Online]. Available: https://academiaromana.ro/sectii2002/proceedings/doc2008-2/08-Bernad.pdf. [Accessed 01 04 2023].

[9] "Canada's energy future is powered by water," Water Powr and Dam Construction, 31 8 2022. [Online]. Available: https://www.waterpowermagazine.com/features/featurecanadas-energy-future-is-powered-by-water-9967922/. [Accessed 1 4 2023].

[10] M. Guney and K. Kaygusuz, "Hydrokinetic energy conversion systems: A technology status review," *Renewable and Sustainable Energy Reviews,* vol. 14, pp. 2996-3004, 2010.

[11] R. Saxena, D. Adhikari and H. Goyal, "Biomass-based energy fuel through biochemical routes: A review," *Renewable and Sustainable Energy Reviews,* vol. 13, no. 1, pp. 167-178, 2009.

[12] "Is Water Really 800 Times More Dense Than Air? We Did the Math," MySwimPro, [Online]. Available: https://blog.myswimpro.com/2023/01/23/is-water-really-800-times-more-dense-than-air-we-did-the-math/. [Accessed 2 4 2023].

[13] A. Betz, Introduction to the Theory of Flow Machines, New York: Pergamon Press, 1966.

[14] P. Coelho, "The Betz limit and the corresponding thermodynamic limit," *Sage Journals,* vol. 47, no. 2, pp. 491-496, 2022.

[15] R. Herschy, "Editorial to: Open channel flow measurement," *Flow Measurement and Instrumentation,* vol. 13, pp. 189-190, 2002.

[16] I. Fujita, Y. Notoya, K. Tani and S. Tateguchi, "Efficient and Accurate Estimation of Water Surface Velocity in STIV," *Environmental Fluid Mechanics,* vol. 19, pp. 1363-1378, 2019.

[17] I. Fujita, T. Deguchi, K. Doi, D. Ogino, S. Tateguchi and Y. Notoya, "DEVELOPMENT OF KU-STIV: SOFTWARE TO MEASURE SURFACE VELOCITY DISTRIBUTION AND DISCHARGE FROM RIVER SURFACE IMAGES," in *Proceedings of the 37th IAHR World Congress,* Kuala Lumpur, 2017.

[18] R. J. Adrian, "Twenty Years of Particle Image Velocimetry," *Experiments in Fluids,* August 2005.

[19] H. Zhao, H. Chen, B. Liu, W. Liu, C.-Y. Xu and S. Guo, "An improvement of the Space-Time Image Velocimetry combined with a new denoising method for estimating river discharge," *Flow Measurement and Instrumentation,* vol. 77, no. 101864, 2021.

[20] M. Muste, I. Fujita and A. Hauet, "Large-scale particle image velocimetry for measurements in riverine environments," *WATER RESOURCES RESEARCH,* vol. 44, no. 4, pp. W00D19-n/a, 2008.

[21] J. L. Coz, A. Hauet, G. Pierrefeu, G. Dramais and B. Camenen, "Performance of image-based velocimetry (LSPIV) applied to flash-flood discharge measurements in Mediterranean rivers," *Journal of Hydrology,* vol. 394, pp. 42-52, 2010.

[22] Q. W. Lewis and B. L. Rhoads, "Resolving two-dimensional flow structure in rivers using large-scale particle image velocimetry: An example from a stream confluence," *Water Resources Research,* pp. 7977-7994, 12 October 2015.

[23] A. Hauet, A. Kruger, W. F. Krajewski, A. Bradley, M. Muste, J.-D. Creutin and M. Wilson, "Experimental System for Real-Time Discharge Estimation Using an Image-Based Method," *JOURNAL OF HYDROLOGIC ENGINEERING,* vol. 13, no. 2, pp. 105-110, 2008.

[24] W. Ahmad and D. Kim, "Estimation of flow in various sizes of streams using the Sentinel-1 Synthetic Aperture Radar (SAR) data in Han River Basin, Korea," *International Journal of Applied Earth Observation and Geoinformation,* vol. 83, no. 6, 2019.

[25] T. N. B. S. o. R. I. Environment, "New Brunswick Ice Manual," Communication New-Brunswick, 2011. [Online]. Available: https://www2.gnb.ca/content/dam/gnb/Departments/env/pdf/Publications/RiverIceManual.pdf. [Accessed 21 10 2023].

[26] S. d'Auteuil, "Investigation of velocity and turbulence measurement techniques for riverine hydrokinetic turbine sites," University of Manitoba, Winnipeg, 2017.

[27] P. J. Pritchard, Fox and McDonald's Introduction to Fluid Mechanics, 8th ed., Manhattan: John Wiley & Sons, Inc., 2011.

[28] P. Koutalakis, O. Tzoraki and G. Zaimes, "UAVs for Hydrologic Scopes: Application of a Low-Cost UAV to Estimate Surface Water Velocity by Using Three Different Image-Based Methods," *Drone,* 28 January 2019.

[29] G. Usera, "Adaptive algorithms for PIV image analyzing," in *Grupo de TrabajoSobreHidromecanica*, 1999.

[30] A. Kruger, A. Bradley, M. Muste and I. Fujita, "Real-Time Measurements of Free-Surface Velocity Using Imaging Techniques," Hydroinformatics 2000, CDROM, 2000.

[31] I. Grant, "Particle image velocimetry: A review," *Sage Journals,* vol. 211, no. 1, pp. 55-76, 1997.

[32] C. Tomaszewski, P. Scerri and J. Dolan, "Augmenting LSPIV Surface Current Measurement with Drifting ASVs," [Online]. Available: https://www.ri.cmu.edu/app/uploads/2019/04/1805-OCEANS-Final.pdf. [Accessed 09 July 2023].

[33] W. M. S. T. Committee, National Industry Guidelines for hydrometric monotoring, Part 11, Commonwealth of Australia (Bureau of Meteorology) , 2020.

[34] M. Muste, A. Hauet, I. Fujita, C. Legout and H.-C. Ho, "Capabilities of Large-scale Particle Image Velocimetry to characterize shallow free-surface flows," *Advances in Water Resources,* no. 70, pp. 160-171, 2014.

[35] I. Fujita, H. Watanabe and R. Tsubaki, "Development of a non-intrusive and efficient flow monitoring technique: The space-time image velocimetry (STIV)," *Intl. J. River Basin Management,* vol. 5, no. 2, pp. 105-114, 2007.

[36] X. Han, K. Chen, Q. Zhong, Q. Chen, F. Wang and D. Li, "Two-Dimensional Space-Time Image Velocimetery for Surface Flow Field of Mountain Rivers Based on UAV Video," *Frontiers in Earth Science,* 28 June 2021.

[37] Q. W. Lewis and B. L. Rhoads, "LSPIV Measurements of Two-Dimensional Flow Structure in Streams Using Small Unmanned Aerial Systems: 2. Hydrodynamic Mapping at River Confluences," *Water Resources Research,* vol. 54, pp. 7981-7999, 2018.

[38] C. C. Chickadel, R. A. Holman and M. H. Freilich, "An optical technique for the measurement of longshore currents," *JOURNAL OF GEOPHYSICAL RESEARCH,* vol. 108, no. C11, p. 3364, 2003.

[39] W. Thielicke and E. J. Stamhuis, "PIVlab – Towards User-friendly, Affordable and Accurate Digital Particle Image Velocimetry in MATLAB," *Journal of open research software,* 2014.

[40] J. Le Coz, A. Hauet, G. Pierrefeu, G. Dramais and B. Camenen, "Performance of image-based velocimetry (LSPIV) applied to flash-flood discharge measurements inMediterranean riversMediterranean rivers," *Journal of Hydrology,* vol. 394, pp. 42-52, 2010.

[41] A. A. Harpold, "Discharge Measurement in Streams Using a Large-Scale Particle Image Velocimetry Prototype," Virginia Polytechnic Institute and State University, Blacksburg, 2005.

[42] M. J. Jolley, A. J. Russell, P. F. Quinn and M. T. Perks, "Considerations When Applying Large-Scale PIV and PTV for Determining River Flow Velocity," Frontiers on Water, 02 December 2021. [Online]. Available: https://www.frontiersin.org/journals/water/articles/10.3389/frwa.2021.709269/full. [Accessed 6 May 2023].

[43] R. Ettema, I. Fujita, M. Muste and A. Kruger, "Particle-image velocimetry for whole-field measurement of ice velocities.," *Cold Regions Science and Technology,* vol. 26, pp. 97-112, 1997.

[44] Z. Zhang, X. Wang, T. Fan and L. Xu, "River surface target enhancement and background suppression for unseeded LSPIV," *Flow Measurement and Instrumentation,* vol. 30, pp. 99-111, 2013.

[45] S. Pena-Haro , B. Luthi, R. Lukes and M. Carrel, "Wind effect on image-based river surface velocity measurements," 4-8 May 2020. [Online]. Available:

https://meetingorganizer.copernicus.org/EGU2020/EGU2020-9943.html. [Accessed 15 July 2023].

[46] A. Daigle, F. Bérubé, . N. Bergeron and P. Matte, "A methodology based on Particle image velocimetry for river ice velocity measurement," *Cold Regions Science and Technology,* vol. 89, pp. 36-47, 2013.

[47] Hydro-STIV Operation Manual, Hydro Technology Institute Co., Ltd., 2023.

[48] I. Fujita, M. Muste and A. Kruger, "Large-scale particle image velocimetry for flow analysis in hydraulic engineering applications," *Journal of Hydraulic Research,* vol. 36, no. 3, pp. 397-414, 2010.

[49] J. Creutin, M. Muste, A. Bradley, S. Kim and A. Kruger, "River gauging using PIV techniques: a proof of concept experiment on the Iowa River," *Journal of Hydrology,* vol. 277, pp. 182-194, 2003.

[50] A. A. Bradley and A. Kruger, "Flow measurement in streams using video imagery," *WATER RESOURCES RESEARCH,* vol. 38, no. 12, p. 1315, 2002.

[51] I. Fujita, M. Muste and A. Kruger, "Large-scale particle image velocimetry for flow analysis in hydraulic engineering applications," *JOURNAL OF HYDRAULIC RESEARCH,* vol. 36, no. 3, pp. 397-414, 1998.

[52] "NADIR Images and Oblique Images in Remote Sensing," GeoSense, [Online]. Available: https://tnmthai.medium.com/nadir-images-and-oblique-images-36ca6c9c4e44. [Accessed 30 July 2023].

[53] I. Fairley, B. J. Williamson, J. McIlvenny, N. King, I. Masters, M. Lewis, . S. Neill, D. Glasby, D. Coles, . B. Powell, K. Naylor, M. Robinson and D. E. Reeve, "Drone-based large-scale particle image velocimetry applied to tidal stream energy resource assessment," *Renewable Energy*, vol. 196, pp. 839-855, 2022.

[54] M. Streßer, R. Carrasco and J. Horstmann, "Video-Based Estimation of Surface Currents Using a Low-Cost Quadcopter," *IEEE GEOSCIENCE AND REMOTE SENSING LETTERS*, vol. 14, no. 11, pp. 2027-2031, 2017.

[55] M. Detert, "How to Avoid and Correct Biased Riverine Surface Image Velocimetry," *Water Resources Research*, 3 November 2020.

[56] E. F. Gökhan, "Dynamic masking techniques for Particle Image Velocimetry," *JOURNAL OF THERMAL SCIENCE AND TECHNOLOGY*, vol. 37, no. 2, pp. 61-74, 2017.

[57] M. Raffel, C. E. Willert, S. T. Wereley and J. Kompenhans, Particle Image Velocimetry: A Practical Guide, Springer, 2007.

[58] C. E. Willert and M. Gharib, "Digital particle image velocimetry," *Experiments in Fluids*, vol. 10, pp. 181-193, 1991.

[59] S. S. Sahu, A. K. S. S. Ghrera and M. Elhoseny, "An approach for de-noising and contrast enhancement of retinal fundus image using CLAHE," *Optics and Laser Technology*, vol. 110, pp. 87-98, 2019.

[60] S. Sudhakar, "Histogram Equalization," Towards Data Science, [Online]. Available: https://towardsdatascience.com/histogram-equalization-5d1013626e64. [Accessed 12 08 2023].

[61] R. C. Gonzales and R. E. Woods, Digital Image Processing, 4th ed., Harlow: Pearson Education Limited, 2018.

[62] U. Shavit, R. J. Lowe and J. V. Steinbuck, "Intensity capping: a simple method to improve cross-correlation piv results Experiments in Fluids," *Exp Fluids,* vol. 42, pp. 225-240, 2007.

[63] E. J. Stamhuis, "Basics and principles of particle image velocimetry (PIV) for mapping biogenic and biologically relevant flows," *Aquatic Ecology,* vol. 40, pp. 463-479, 2006.

[64] J. Nogueira, A. Lecuona and P. A. Rodr´ıguez, "Data validation, false vectors correction and derived magnitudes calculation on PIV data," *Measurement Science and Technology,* vol. 8, pp. 1493-1501, 1997.

[65] C. Masafu, R. Williams, X. Shi, Q. Yuan and M. Trigg, "Unpiloted Aerial Vehicle (UAV) image velocimetry for validation of two-dimensional hydraulic model simulations," *Journal of Hydrology,* vol. 612, 2022.

[66] D. Garcia, "Robust smoothing of gridded data in one and higher dimensions with missing values," *Computational Statistics and Data Analysis,* vol. 54, pp. 1167-1178, 2010.

[67] "Phantom 3," DJI, [Online]. Available: https://www.dji.com/ca/phantom-3-pro. [Accessed 16 04 2023].

[68] "Flying your drone safely and legally," Government of Canada, [Online]. Available: https://tc.canada.ca/en/aviation/drone-safety/learn-rules-you-fly-your-drone/flying-your-drone-safely-legally. [Accessed 02 08 2023].

[69] T. H. Yorke and K. A. Oberg, "Measuring river velocity and discharge with acoustic Doppler profilers," *Flow Measurement and Instrumentation,* vol. 13, pp. 191-195, 2002.

[70] R. Kostaschuk, J. Best, P. Villard, J. Peakall and M. Franklin, "Measuring flow velocity and sediment transport with an acoustic Doppler current profiler," *Geomorphology,* vol. 68, pp. 25-37, 2005.

[71] D. Pumo, F. Alongi, G. Ciraolo and L. V. Noto, "Optical Methods for River Monitoring: A Simulation-Based Approach to Explore Optimal Experimental Setup for LSPIV," *Water,* vol. 13, no. 247, 2021.

[72] J. Westerweel, D. Dabiri and . M. Gharib, "The effect of a discrete window offset on the accuracy of cross-correlation analysis of digital PIV recordings," *Experiments in Fluids,* vol. 23, pp. 20-28, 1997.

[73] H. Huang, D. Dabiri and M. Gharib, "On errors of digital particle image velocimetry," *Measurement Science and Technology,* vol. 8, no. 12, pp. 1427-1440, 1997.

[74] W. Thielicke, *PIVlab - Background and quick start guide,* Youtube, 2018.

[75] "Open Souce Particle Image Velocimetry," OpenPIV, [Online]. Available: http://www.openpiv.net/index.html. [Accessed 5 September 2023].

[76] A. O. Acheampong, "Modelling for insight: Does financial development improve environmental quality?," *Energy Economics,* vol. 83, pp. 156-179, September 2019.

[77] C. Raghutla, P. Padmagirisan, P. Sakthivel and K. R. Chittedi, "The effect of renewable energy consumption on ecological footprint in N-11 countries: Evidence from Panel Quantile Regression Approach," *Renewable Energy,* vol. 197, pp. 125-137, September 2022.

[78] R. Ferris, "Megacities: Making giant urban areas less energy-hungry," 30 April 2015. [Online]. Available: https://www.cnbc.com/2015/04/30/megacities-making-giant-urban-areas-less-energy-hungry.html. [Accessed 10 October 2022].

[79] J. Wood, "Here's what you need to know about the megacities of the future," 10 October 2018. [Online]. Available: https://www.weforum.org/agenda/2018/10/these-are-the-megacities-of-the-future/. [Accessed 10 October 2022].

[80] H. Gronkiewicz-Waltz, A. Larsson and A. Boni, "100 Climate-Neutral Cities by 2030—By and for the Citizens: Report of the Mission Board for Climate-Neutral and Smart Cities, Publications Office. 2020," European Commission, Brussels, 2020.

[81] X. Masip, E. Fuster-Palop, C. Prades-Gil, J. D. Viana-Fons and J. Paya, "Case study of electric and DHW energy communities in a Mediterranean district," *Renewable and Sustainable Energy Reviews,* vol. 178, no. 113234, 2023.

[82] B. Kirke, "Developments in ducted water current turbines," 1 1 2003. [Online]. Available: https://www.researchgate.net/publication/237809015_Developments_in_ducted_water_current_turbines_This_paper_was_originally_written_in_2003_and_published_on_wwwcyberiadnet_This_version_includes_some_updates_on_tests_conducted_in_2005. [Accessed 2 4 2023].

[83] R. Bedard, "Proceedings of the Hydrokinetic and Wave Energy Technologies Technical and Environmental Issues Workshop," 24 3 2006. [Online]. Available: https://www.energy.gov/sites/default/files/2013/12/f5/doewater-102005.pdf. [Accessed 2 4 2023].

[84] "Estimating Open Channel Flow Rate (Float Method)," Intermountain Environmental, Inc., [Online]. Available: https://www.inmtn.com/tools/float-method/. [Accessed 5 08 2023].

[85] J. P. Leitão, S. Peña-Haro, B. Lüthi, A. Scheidegger and M. Moy de Vitry, "Urban overland runoff velocity measurement with consumer-grade surveillance cameras and surface structure image velocimetry," *Journal of Hydrology,* vol. 565, pp. 791-804, 2018.

[86] inforyan, "CLAHE Histogram Equalization – OpenCV," GeeksforGeeks, [Online]. Available: https://www.geeksforgeeks.org/clahe-histogram-eqalization-opencv/. [Accessed 9 August 2023].